Quantum-circuit refrigeration by noise

Heidi Kivijärvi

School of Science

Thesis submitted for examination for the degree of Master of Science in Technology.

Espoo 6.1.2024

Supervisor

Prof. Mikko Möttönen

Advisor

D.Sc. Arto Viitanen

Aalto University
School of Science

Aalto University
School of Science

Aalto University, P.O. BOX 11000, 00076 AALTO
www.aalto.fi
Abstract of the master's thesis

Author Heidi Kivijärvi

Title Quantum-circuit refrigeration by noise

Degree programme Master's Programme in Engineering Physics

Major Materials Physics and Quantum Technology **Code of major** SCI3107

Supervisor Prof. Mikko Möttönen

Advisor D.Sc. Arto Viitanen

Date 6.1.2024 **Number of pages** 46 **Language** English

Abstract

Superconducting quantum computers have emerged as a popular field of research during the recent years, showing rapid improvement in qubit quality and scalability. As the number of qubits on a quantum processor increases, more attention needs to be focused on fast and accurate qubit initialization and reasonable power consumption of the quantum circuits. To address these challenges, the ability of a quantum-circuit refrigerator to initialize a qubit by providing local cooling to its environment can be combined with energy harvested from thermal activation.

The operation of this kind of a Brownian quantum-circuit refrigerator is based on absorption of photons from the refrigerated component promoting photon-assisted tunneling events through a normal-metal–insulator–superconductor tunnel junction. Since the activation energy of tunneling is typically large compared to the energy of photons originating from the component, the remaining energy needed for tunneling is provided by the photons arising from thermal voltage fluctuations in the circuit. Thus, the Brownian refrigerator can harness redundant thermal fluctuations for practical use to cool these components by lowering their photon occupation.

This thesis investigates the effect of a noise-driven quantum-circuit refrigerator on the coherent and thermal states of a coupled resonator. By exploiting a transmon qubit as a dispersive probe, we experimentally demonstrate the suppression of the mean photon number and equivalent temperature of the resonator owing to the activation of photon-assisted tunneling by artificial noise. Based on these results, the utilization of noise from a true thermal source arises as a natural step.

Keywords quantum-circuit refrigerator, QCR, noise, Brownian refrigerator

Aalto University
School of Science

Aalto-yliopisto, PL 11000, 00076 AALTO
www.aalto.fi
Diplomityön tiivistelmä

Tekijä Heidi Kivijärvi

Työn nimi Kvanttipiirijäähdytys kohinalla

Koulutusohjelma Master's Programme in Engineering Physics

Pääaine Materials Physics and Quantum Technology **Pääaineen koodi** SCI3107

Työn valvoja Prof. Mikko Möttönen

Työn ohjaaja TkT Arto Viitanen

Päivämäärä 6.1.2024 **Sivumäärä** 46 **Kieli** Englanti

Tiivistelmä

Suprajohtava kvanttitietokone on noussut suosituksi tutkimusalaksi viime vuosien aikana, osoittaen nopeaa kehitystä kubittien laadussa ja skaalautuvuudessa. Kvanttiprosessorien kubittimäärän kasvaessa on kohdennettava enemmän huomiota kubittien nopeaan ja tarkkaan alustamiseen sekä kvanttipiirien kohtuulliseen tehonkulutukseen. Näihin haasteisiin voidaan mahdollisesti vastata yhdistämällä kvanttipiirijäähdyttimen kyky alustaa kubitti jäähdyttämällä lokaalia ympäristöään ja termisestä alkuperästä juontuva aktivoituminen.

Tällaisen Brownin kvanttipiirijäähdyttimen toiminta perustuu fotonien absorboitumiseen jäähdytettävästä komponentista fotoniavusteisessa tunneloitumisprosessissa normaalimetalli–eriste–suprajohdetunneliliitoksen läpi. Tunneloitumisen aktivoimiseen vaadittavan energian ollessa tyypillisesti suuri verrattuna komponentista peräisin olevien fotonien energiaan tarvittava jäljelle jäävä energia saadaan fotoneista, jotka syntyvät virtapiirin termisestä jännitekohinasta. Näin Brownin jäähdytin kykenee valjastamaan hukkalämmön hyötykäyttöön näiden komponenttien jäähdyttämiseen alentamalla niiden fotonimiehitystä.

Tämä diplomityö tarkastelee kohinalla ajetun kvanttipiirijäähdyttimen vaikutusta siihen kytkeytyneen resonaattorin koherentteihin ja termisiin tiloihin. Käyttämällä hyödyksi transmonkubittia dispersiivistä siirtymää hyödyntävänä ilmaisimena osoitamme kokeellisten tulosten kautta resonaattorin keskimääräisen fotoniluvun ja ekvivalenttilämpötilan pienentymisen keinotekoisen kohinan aktivoidessa fotoniavusteisen tunneloitumisen. Näiden tulosten perusteella aitoon lämpöliikkeeseen perustuvan kohinalähteen hyödyntäminen toimii luonnollisesti seuraavana askeleena.

Avainsanat kvanttipiirijäähdytin, QCR, kohina, Brownin jäähdytin

Preface

The work resulting in this master's thesis was carried out in the QCD group at Aalto University's Department of Applied Physics during the latter half of 2023. First, I would like to thank my advisor D.Sc. Arto Viitanen for sharing his vast knowledge of the QCR, getting me started with the experiments, and always being ready to help and answer any questions. I would also like to thank M.Sc Timm Mörstedt for sharing his honorably long-lasting sample for my experiments and for sharing his experience and knowledge of nanofabrication. Finally, I would like to thank Prof. Mikko Möttönen for providing me a fantastic learning path via the previous projects to this point of my academic career in an encouraging and well-resourced environment.

Espoo, 12.12.2023 Heidi Kivijärvi

Contents

Abstract i

Abstract (in Finnish) ii

Preface iii

Contents iv

1 Introduction 1

2 Theoretical background 3
- 2.1 Photon-assisted tunneling through an NIS junction 3
- 2.2 Quantum-circuit refrigerator 5
- 2.3 Circuit quantum electrodynamics 6
  - 2.3.1 Circuit Lagrangian 6
  - 2.3.2 System Hamiltonian 9
  - 2.3.3 Diagonalization of the core Hamiltonian 10
  - 2.3.4 Microscopic Hamiltonian 10
  - 2.3.5 Tunneling matrix elements 12
  - 2.3.6 Tunneling rates 13
  - 2.3.7 Resonator transition rate 14
  - 2.3.8 Characteristic parameters 15
- 2.4 Quantum Brownian refrigerator 16
- 2.5 Dispersive readout with a transmon qubit 17

3 Sample layout and fabrication 20
- 3.1 Sample structure 20
- 3.2 Fabrication process 21

4 Experimental methods 23
- 4.1 Measurement setup 23
- 4.2 Measurement protocol 25

5 Results 27
- 5.1 Characterization of the device 27
- 5.2 Analog frequency-modulated drive of the resonator 35
- 5.3 Analog frequency-modulated drive of the QCR 36
- 5.4 Vector frequency-modulated drive 38

6 Summary and outlook 42

References 43

1 Introduction

In only four decades, quantum computing has evolved from a futuristic concept, first described by Benioff [1] and Feynman [2], into a reality of actual multi-qubit quantum processors [3, 4], public cloud-based access to quantum computing resources [5, 6], and an established research field firmly in pursuit of universal quantum advantage [7]. However, the current state-of-the-art quantum-processor technology is still faced with unresolved obstacles that hinder the scale-up of the hardware towards solving practical tasks. Superconducting qubits are currently among the most popular choices for implementing quantum processors, due to the rapid improvement in qubit quality and scalability during the recent years, as well as their designability and simple coupling and control based on circuit quantum electrodynamics (cQED) [8, 9]. Coherence time, the quasi-two-level nature facilitating also undesired transitions, and the necessity of cryogenic operating temperatures are the essential characteristics that still require attention to unleash the full potential of scalable superconducting quantum computing.

Even at cryogenic temperatures, the presence of the electromagnetic environment inflicts qubit decoherence, leading to computational errors. On the other hand, the readout and control of superconducting qubits rely on the very same environmental coupling, thus, a real qubit cannot be completely isolated from its surroundings. Hence, the use of efficient error correction protocols is necessary, which require fast and accurate initialization of ancilla qubits [10–12].

In order to reach the usual operating temperatures of superconducting circuits in the subkelvin range, typically a dilution refrigerator is used. However, transmitting power from a room-temperature source through a set of room-temperature and cryogenic attenuators to the millikelvin quantum circuit inside the refrigerator, using separate cables for the control and readout of each individual qubit, is highly inefficient from the perspective of both power consumption and space utilization. Realization of a novel group of devices [13–17] that exploit thermal energy from the environment as their power source aims to improve the efficiency and scalability of superconducting quantum circuits.

In this thesis, we consider a Brownian refrigerator [18], an autonomous device that utilizes thermal noise from a hot source to provide in-situ cooling to its local environment. Previously, Brownian refrigeration of electrons in hybrid tunnel junctions has been proposed in Ref. [17]. Here, our focus lies on cooling the relevant modes of a quantum circuit by photon absorption, which is activated by thermal noise from the environment. To this end, we utilize the extensively studied quantum-circuit refrigerator (QCR) [19, 20], which has recently been demonstrated to provide tunable dissipation for resonators [21–24], involve an alternative operating mode as an incoherent photon source [25], and enable fast initialization of superconducting qubits [26, 27].

The cooling effect of the QCR is based on the absorption of photons from the environment in photon-assisted tunneling (PAT) of electron-like quasiparticles through a normal-metal–insulator–superconductor (NIS) junction [20]. The QCR allows for various activation schemes, including dc voltage biasing [19, 28], microwave pulsing [22, 26, 27], and the driven supportive mode of a coupled resonator [23, 29].

The aim of this thesis is to experimentally study the characteristics of the QCR powered by noise, mimicking the operation of a quantum Brownian refrigerator (QBR). This type of device provides auspicious prospects for the future of superconducting quantum computing by combining the potential of the QCR in fast initialization with the energy efficiency and scalability arising from the utilization of the thermal energy of the environment. The thesis is divided into several parts. We begin by introducing the theoretical background in Sec. 2, needed to understand the physics behind the experimentally observed phenomena. Section 3 provides an overview of the sample used in the experimental part of this thesis, followed by a description of the experimental setup and methods in Sec. 4. The experimental results and their analysis is presented in Sec. 5, and finally, the main conclusions of this thesis are summarized together with future prospects in Sec. 6.

2 Theoretical background

In this chapter, we discuss the relevant theory behind the operation of the thermally driven QCR. We begin by introducing the concept of photon-assisted tunneling through hybrid tunnel junctions in Sec. 2.1. A direct application of PAT in refrigerating quantum circuits and different biasing schemes of the QCR are discussed in Sec. 2.2. Next, in Sec. 2.3, we present the general mathematical tools for describing a QCR coupled to a resonator, as given by the cQED approach. After that, we move on to discuss the concept and characteristics of QBR in Sec. 2.4. Finally, in Sec. 2.5, we consider a resonator readout scheme that utilizes a transmon qubit as a dispersive probe.

2.1 Photon-assisted tunneling through an NIS junction

Tunneling of charged particles is a purely quantum-mechanical phenomenon, in which a particle has a finite probability to penetrate through a thin potential barrier, contrary to the total reflection given by the classical approach [30]. In the context of QBR, we consider tunneling through an NIS junction, comprising a normal-metal electrode and a superconducting electrode, separated by a thin insulator with a typical thickness of the order of a nanometer [31, 32].

In the most typical case, the tunnel junction is biased by applying a dc voltage V between the two electrodes, thus modifying their electrochemical potential difference by eV, where e is the elementary charge. The superconducting electrode accommodates Cooper pairs as current-carrying particles, as given by the BCS theory [33]. The quasiparticle density of states of a superconductor is gapped, implying that scattering within the energy range of 2Δ around the Fermi level, where Δ is the superconductor gap parameter, is forbidden. Consequently, in the unbiased case, tunneling of an electron from the normal-metal electrode requires an additional energy Δ to reach available single-particle states, rendering the tunneling particles as electron-like Bogoliubov quasiparticles. Since the other electrode is in a normal-metallic state, tunneling of Cooper pairs is suppressed. Figure 1 illustrates the relevant tunneling processes present in the biased NIS junction.

Typically, the junction is coupled to an electromagnetic environment, such as a qubit or a resonator, that can provide or receive photons that are absorbed or emitted during the tunneling event. At low bias voltages the Fermi level of the normal electrode lies within the superconductor gap, as illustrated in Fig. 1(a). Therefore, elastic tunneling, in which the energy of the particle is conserved, is suppressed. Similarly, tunneling that involves emission of photons is suppressed due to the lack of available states. If the energy and the number of photons in the environment of the junction is small, tunneling that involves photon absorption is also suppressed, and the junction is in the off state, passing essentially no tunneling current. The tunneling processes that involve either photon absorption or emission are referred to as photon-assisted tunneling.

If the junction is biased sufficiently close to the gap edge, elastic tunneling is still suppressed, but the electron may absorb a photon from the environment to

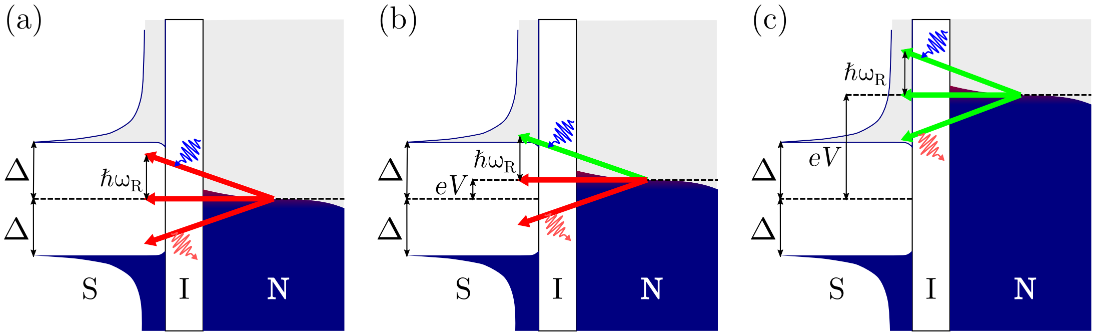

Figure 1: Schematic illustration of the relevant tunneling processes in an NIS junction from the normal electrode to the superconducting electrode. The Fermi levels of the electrodes, separated by a bias-voltage-dependent energy eV, are marked with dashed lines. The blue (gray) shaded regions indicate filled (empty) states. The three arrows denote the different tunneling processes: tunneling with photon absorption (top), elastic tunneling (middle), and tunneling with photon emission (bottom). The energy of the photon is given by $\hbar\omega_{\rm R}$. The green (red) color represents a process that is energetically allowed (forbidden) in the respective bias state. (a) In the non-biased case, all tunneling processes are suppressed and negligible current is passing through the junction. (b) When the junction is biased near the gap edge Δ, photon absorption is required to enable tunneling. (c) In the high-bias case, all three processes are possible.

reach a total energy $eV + \hbar\omega_{\rm R} \geq \Delta$, where $\hbar$ is the reduced Planck constant and $\omega_{\rm R}/(2\pi)$ is the frequency of the photon, enabling its tunneling as a quasiparticle to the superconducting electrode. This biasing scheme is illustrated in Fig. 1(b). Consequently, the environment of the junction is cooled in the process owing to the decrease in photon number.

At high bias voltages $eV \geq \Delta$, all three tunneling processes described above are possible, as shown in Fig. 1(c). However, at usual experimental conditions, elastic tunneling dominates over the inelastic processes [20]. Furthermore, above the gap, the rate of tunneling that involves photon emission tends to increase faster than the absorption rate as a function of bias voltage, thus it is possible to reach a bias configuration, in which the junction acts as a net source of photons [20, 25]. The transition rates associated with different tunneling processes are further discussed in Sec. 2.3.

In our calculations, tunneling of charged particles is considered within the first-order perturbation theory. The transition rates are then straightforwardly obtained from the Fermi golden rule [34]

$$\Gamma_{i\to f} = \frac{2\pi}{\hbar} \left| \langle f | \hat{H}_{\rm T} | i \rangle \right|^2 \delta(E_f - E_i), \tag{1}$$

where i (f) is the initial (final) state with the associated energy E_i (E_f), $\hat{H}_{\rm T}$ is the tunneling Hamiltonian, and $\delta(E)$ is the Dirac delta distribution. Following the standard derivation [34], the general form for the total forward tunneling rate from the first electrode to the second electrode becomes

$$\overrightarrow{\Gamma}_{1\to 2}(V) = \frac{1}{e^2 R_\mathrm{T}} \int_{\infty}^{\infty} \int_{\infty}^{\infty} \mathrm{d}E\mathrm{d}E' n_1(E) n_2(E'-eV) f_1(E)[1-f_2(E'-eV)] P(E-E'), \tag{2}$$

where R_T is the tunneling resistance of the junction, $V = V_1 - V_2$ is the bias voltage between the two electrodes, $f_j(E) = \frac{1}{\exp[E/(k_\mathrm{B}T_j)]+1}$ is the Fermi–Dirac distribution of electrode j, and $P(E)$ is the probability density function for the environment to absorb the amount of energy $E > 0$. The normalized density of states $n_j(E)$ is defined as $n_N(E) = 1$ for the normal electrode and

$$n_\mathrm{S}(E) = \left| \mathbb{R} \left\{ \frac{E + \mathrm{i}\eta}{\sqrt{(E+\mathrm{i}\eta)^2 - \Delta^2}} \right\} \right|, \tag{3}$$

for the superconducting electrode [35–37], where i is the imaginary unit and η is the Dynes parameter, which expresses, for example, the finite lifetime of quasiparticles.

The physical interpretation of the tunneling rate formula in Eq. (2) is simple. The term $n_1(E)f_1(E)$ describes the quasiparticles occupying a state with energy E on the first electrode, whereas $n_2(E' - eV)[1 - f_2(E' - eV)]$ describes the unoccupied states with energy $E' - eV$ on the second electrode, to which the quasiparticles may tunnel after gaining an energy $-eV$ due to the bias voltage. The term $P(E - E')$ describes the probability of absorbing ($E < E'$) or emitting ($E > E'$) a photon with energy $E - E'$ during the tunneling process. In the limit of low impedance environment, the probability function reduces to a delta function $P(E - E') = \delta(E - E')$, in which case only elastic tunneling $E' = E$ is possible [34].

2.2 Quantum-circuit refrigerator

As discussed in the previous section, an NIS junction can cool its environment by absorbing photons in the PAT process. This feature is exploited by a quantum-circuit refrigerator to locally cool down the critical components of a quantum circuit. In its original proposal and in most of the previous research, the QCR consists of a double-junction SINIS-structure, in which a normal-metal island between the junctions is capacitively coupled to the target component [19, 22, 23, 25–27]. In this configuration, the voltage biasing of the double-junction and the designability of the coupled circuit is straightforward. However, the island structure is subject to slow charging dynamics, degrading the QCR-induced energy decay of the coupled system [38]. In this thesis, we study a more recently developed type of a QCR [24, 28], in which a quarter-wave coplanar-waveguide resonator provides a direct-current path to ground for a single NIS junction. Consequently, the absence of the charge island is expected to improve the decay dynamics of the system compared to the double-junction design. The layout of this configuration is discussed in more detail in Sec. 3.1.

The cooling effect on the environment can be demonstrated in a versatile manner by coupling the QCR to a microwave resonator. In the single-junction configuration, this coupling is inherently realized. The resonator coupling is advantageous also in the sense that it can mediate a coupling between the QCR and other circuit components, such as qubits. To this end, the resonator was recently demonstrated to provide further enhancement of the decay rate of a QCR-cooled superconducting qubit [27].

Typically, the QCR is powered using a dc voltage applied over the junction, as described in the previous section, to excite the quasiparticles close to the gap edge, so that photon absorption from the resonator activates the tunneling process. Another option that has been demonstrated recently utilizes a driven second mode of the resonator [23]. In this powering scheme, the QCR absorbs two photons: one from the primary mode which we aim to cool, and one from the driven secondary mode. Thus the required dc bias voltage is smaller by the secondary photon energy. Moreover, by increasing the driving power of the secondary mode, we can increase the photon population of the mode to activate multiphoton-assisted tunneling, in which multiple secondary photons are absorbed in the tunneling process, replacing an even larger proportion of the dc bias voltage.

Furthermore, the dc bias voltage can be replaced by a direct rf drive of the QCR [24]. In this case, the secondary photons are provided by the electromagnetic field from the QCR side, instead of driving the resonator. An extension of this powering scheme, and the interest of this thesis, is to drive the QCR using noise. Here, we use artificially generated rf noise created by a signal generator, which is a step towards powering the QCR purely by random thermal noise from the environment. This type of device could be rendered as a quantum Brownian refrigerator, which is discussed further in Sec. 2.4.

2.3 Circuit quantum electrodynamics

Circuit quantum electrodynamics [39] describes the light–matter interactions and quantum nature arising from electric circuits. In the context of quantum-circuit refrigeration, we elaborate the operation of a single-junction QCR coupled to a microwave resonator by deriving the system Hamiltonian and transition rates for the corresponding lumped-element circuit, using the general approach of cQED. This derivation differs from the standard $P(E)$-theory used in Sec. 2.1, and leads to a more detailed formulation of the transition rates in terms of the number of photons involved. Furthermore, the cQED approach presented here is general in the sense that it considers an arbitrary QCR with a normal-metal island, and, therefore, naturally extends to describe a double-junction QCR. By applying certain assumptions, the final result for the island-free single-junction QCR can be obtained as a special case.

2.3.1 Circuit Lagrangian

The analytical formulation of an electric circuit is obtained by considering the circuit as a network of electric components residing in branches that connect at specific nodes. The components are characterized by two branch variables, branch voltage v_{b} and branch current i_{b}. These variables are related to branch flux ϕ_{b} and branch charge $q_{\rm b}$ via integration [40]

$$\phi_{\rm b}(t) = \int_{-\infty}^{t} v_{\rm b}(\tau)\mathrm{d}\tau, \tag{4}$$

$$q_{\rm b}(t) = \int_{-\infty}^{t} i_{\rm b}(\tau)\mathrm{d}\tau. \tag{5}$$

For linear capacitive and inductive components considered here, we also have

$$i_{\rm b}(t) = \frac{\phi_{\rm b}(t)}{L_{\rm b}}, \tag{6}$$

$$v_{\rm b}(t) = \frac{q_{\rm b}(t)}{C_{\rm b}}, \tag{7}$$

where $L_{\rm b}$ is the branch inductance and $C_{\rm b}$ is the branch capacitance. Here, the mutual inductances from other branches are neglected [40].

A lumped-element circuit diagram illustrating a QCR capacitively coupled to a resonator is shown in Fig. 2(a). In the lumped-element approach, the QCR is modeled as a capacitor $C_{\rm j}$ in parallel with the NIS junction. Here, we first consider the normal-metal lead as a charge island, which is coupled to the ground and to the resonator with capacitances $C_{\rm m}$ and $C_{\rm C}$, respectively. In the case of a double-junction QCR, the effect of the second junction would be included in the value of island-to-ground capacitance $C_{\rm m}$. The resonator is characterized by capacitance C and inductance L. The coupling of the QCR circuit to a secondary circuit, covering components such as transmission lines or a qubit, is denoted by capacitance $C_{\rm g}$.

The characteristic impedance of a transmission line appears as an effective renormalization of the resonator capacitance and frequency [20], but does not further affect the electrodynamics of the circuit. Thus, we consider the renormalization to be included in the values C and $\omega_{\rm R}$ of the resonator. On the other hand, the presence of a qubit in the secondary circuit will slightly alter the general form of the transition rates due to the strong dispersive coupling to the resonator [38]. However, here we only consider the more dominant transition processes, in which the resonator state may change but the qubit state is fixed. Consequently, the relevant transition rates simplify into the same form as derived for the non-coupled primary circuit. Thus, for a secondary circuit comprising only transmission lines or transmission lines and a qubit, we may neglect the coupling capacitance $C_{\rm g}$ in the derivation of the relevant transition rates.

In order to formulate the Lagrangian operator for the QCR–resonator system, we define a spanning tree for the circuit topology [40], as illustrated in Fig. 2(b). First, we introduce a reference ground node $(Q_0, \Phi_0) = (0, 0)$, characterized by node charge and node flux, respectively. Then, we choose two active nodes: the QCR island node $(Q_{\rm N}, \Phi_{\rm N})$ and the resonator node (Q, Φ). In order to simplify the derivation, we temporarily approximate the voltage source V as a capacitor $C_{\rm V}$ and associate with it an auxiliary active node $(Q_{\rm V}, \Phi_{\rm V})$. The spanning tree is constructed by connecting each active node to the reference node by a single path defined by the branches. The remaining closure branches define a set of loops by connecting the paths along the

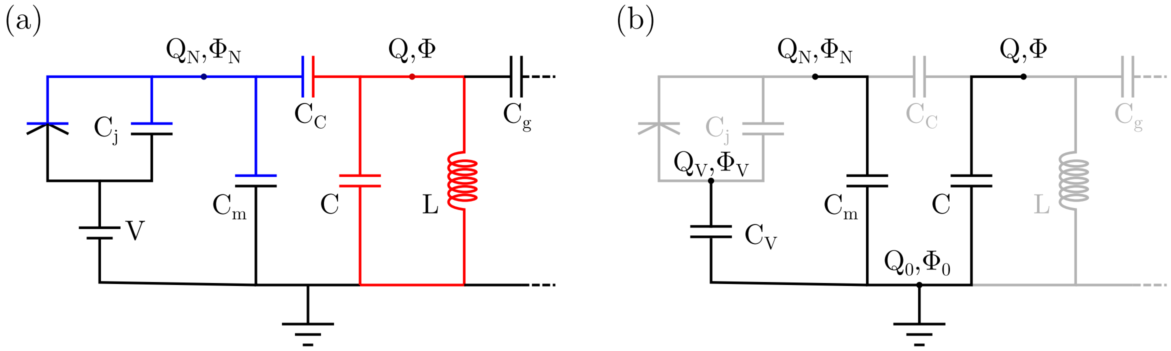

Figure 2: (a) Lumped-element circuit diagram of a QCR coupled to a resonator characterized by capacitance C and inductance L. The normal metal island of the QCR is denoted by blue color, and the resonator is denoted by red. The node charge and node flux are given by $Q_{\rm N}$ and $\Phi_{\rm N}$ for the island and by Q and Φ for the resonator, respectively. The capacitance and bias voltage of the NIS junction are denoted by $C_{\rm j}$ and V, respectively. The coupling of the island to ground and to the resonator are characterized by capacitances $C_{\rm m}$ and $C_{\rm C}$, respectively. The capacitance $C_{\rm g}$ indicates the coupling to a secondary circuit. (b) The spanning tree (black) of the lumped-element circuit. The closure branches are marked with gray color. The voltage source is approximated as a capacitor $C_{\rm V}$. The auxiliary node for the voltage source and the reference ground node are characterized by charges $Q_{\rm V}$ and Q_0 and fluxes $\Phi_{\rm V}$ and Φ_0, respectively.

spanning tree. In the absence of static fluxes through the loops, the branch flux over a capacitive or inductive component is given by the fluxes of the two end nodes

$$\phi_{\rm b}^{\rm n\to n'} = \Phi_{\rm n'} - \Phi_{\rm n}. \tag{8}$$

Utilizing Eqs. (4)–(8), we obtain the branch current over a capacitor or an inductor respectively as

$$i_{\rm b,C}^{\rm n\to n'} = C_{\rm b}(\ddot{\Phi}_{\rm n'} - \ddot{\Phi}_{\rm n}), \tag{9}$$

$$i_{\rm b,L}^{\rm n\to n'} = \frac{\Phi_{\rm n'} - \Phi_{\rm n}}{L_{\rm b}}. \tag{10}$$

Consequently, the equations of motion for the circuit are obtained by applying Kirchhoff's current law. That is, we equate the sum of all coinciding capacitive and inductive branch currents of Eqs. (9) and (10) to zero for each active node

$$\left\{\begin{array}{rcl} 2C_{\rm C}(\ddot{\Phi}_{\rm N} - \ddot{\Phi}) - C\ddot{\Phi} & = & \dfrac{\Phi}{L} \\ C_{\rm j}(\ddot{\Phi}_{\rm N} - \ddot{\Phi}_{\rm V}) + C_{\rm C}(\ddot{\Phi}_{\rm N} - \ddot{\Phi}) + C_{\rm m}\ddot{\Phi}_{\rm N} & = & 0 \\ C_{\rm V}\ddot{\Phi}_{\rm V} - C_{\rm j}(\ddot{\Phi}_{\rm N} - \ddot{\Phi}_{\rm V}) & = & 0. \end{array}\right. \tag{11}$$

Utilizing the standard definition of Euler–Lagrange equations, we can show that the set of equations (11) correspond to a Lagrangian

$$\mathcal{L} = \frac{C_\mathrm{j}(\dot{\Phi}_\mathrm{N} - \dot{\Phi}_\mathrm{V})^2}{2} + \frac{C_\mathrm{C}(\dot{\Phi}_\mathrm{N} - \dot{\Phi})^2}{2} + \frac{C\dot{\Phi}^2}{2} + \frac{C_\mathrm{m}\dot{\Phi}_\mathrm{N}^2}{2} + \frac{C_\mathrm{V}\dot{\Phi}_\mathrm{V}^2}{2} - \frac{\Phi^2}{2L}. \tag{12}$$

Next, we fix the auxiliary flux back to voltage $\dot{\Phi}_\mathrm{V} = V$ and neglect the irrelevant constant term to obtain the full circuit Lagrangian [20]

$$\mathcal{L} = \frac{C_\mathrm{j}(\dot{\Phi}_\mathrm{N} - V)^2}{2} + \frac{C_\mathrm{C}(\dot{\Phi}_\mathrm{N} - \dot{\Phi})^2}{2} + \frac{C\dot{\Phi}^2}{2} + \frac{C_\mathrm{m}\dot{\Phi}_\mathrm{N}^2}{2} - \frac{\Phi^2}{2L}. \tag{13}$$

2.3.2 System Hamiltonian

The obtained Lagrangian in Eq. (13) can be transformed into the classical Hamiltonian by utilizing the Legendre transformation

$$H_0 = -\mathcal{L} + \sum_i \Phi_i \frac{\partial \mathcal{L}}{\partial \dot{\Phi}_i}, \tag{14}$$

where we apply the conjugate node charges $Q_\mathrm{N} = \frac{\partial \mathcal{L}}{\partial \dot{\Phi}_\mathrm{N}}$ and $Q = \frac{\partial \mathcal{L}}{\partial \dot{\Phi}}$. The Hamiltonian then becomes

$$H_0 = \frac{C_\mathrm{j}}{2}\dot{\Phi}_\mathrm{N}^2 - \frac{C_\mathrm{j}}{2}V^2 + \frac{C_\mathrm{m}}{2}\dot{\Phi}_\mathrm{N}^2 + \frac{C_\mathrm{C}}{2}\dot{\Phi}_\mathrm{N}^2 - C_\mathrm{C}\dot{\Phi}_\mathrm{N}\dot{\Phi} + \frac{C_\mathrm{C}}{2}\dot{\Phi}^2 + \frac{C}{2}\dot{\Phi}^2 + \frac{\Phi^2}{2L}. \tag{15}$$

We then introduce renormalized capacitances for the QCR island and the resonator

$$C_\mathrm{N} = C_\Sigma + C_\mathrm{C} = C_\mathrm{j} + C_\mathrm{m} + C_\mathrm{C}, \tag{16}$$

$$C_\mathrm{R} = C + \alpha C_\Sigma = C + \alpha(C_\mathrm{j} + C_\mathrm{m}), \tag{17}$$

respectively, where $\alpha = \frac{C_\mathrm{C}}{C_\mathrm{N}}$ is the capacitance ratio imposed by the coupling. Utilizing Eqs. (16) and (17) and the definition of the conjugate charges, the classical Hamiltonian can be written in the form

$$H_0 = \frac{(Q_\mathrm{N} + C_\mathrm{j}V)^2}{2C_\mathrm{N}} + \frac{[Q + \alpha(Q_\mathrm{N} + C_\mathrm{j}V)]^2}{2C_\mathrm{R}} + \frac{\Phi^2}{2L} - \frac{C_\mathrm{j}}{2}V^2. \tag{18}$$

After replacing the node charges and fluxes with the corresponding quantized operators and ignoring the irrelevant constant $\frac{C_\mathrm{j}}{2}V^2$, we finally arrive at the core Hamiltonian operator [20]

$$\hat{H}_{0,V} = \frac{(\hat{Q}_\mathrm{N} + C_\mathrm{j}V)^2}{2C_\mathrm{N}} + \frac{[\hat{Q} + \alpha(\hat{Q}_\mathrm{N} + C_\mathrm{j}V)]^2}{2C_\mathrm{R}} + \frac{\hat{\Phi}^2}{2L}. \tag{19}$$

Additionally, the constant charge shift caused by the bias voltage can be eliminated by applying a gauge transformation $|\psi\rangle = \mathrm{e}^{\frac{\mathrm{i}}{\hbar}C_\mathrm{j}V\hat{\Phi}_\mathrm{N}}|\psi\rangle_\mathrm{V}$. Utilizing the commutation relation $[\hat{\Phi}_\mathrm{N}, \hat{Q}_\mathrm{N}] = \mathrm{i}\hbar$ we obtain a simplified core Hamiltonian

$$\begin{aligned} \hat{H}_0 &= \mathrm{e}^{\frac{\mathrm{i}}{\hbar}C_\mathrm{j}V\hat{\Phi}_\mathrm{N}}\hat{H}_{0,\mathrm{V}}\mathrm{e}^{-\frac{\mathrm{i}}{\hbar}C_\mathrm{j}V\hat{\Phi}_\mathrm{N}} \\ &= \frac{\hat{Q}_\mathrm{N}^2}{2C_\mathrm{N}} + \frac{(\hat{Q} + \alpha\hat{Q}_\mathrm{N})^2}{2C_\mathrm{R}} + \frac{\hat{\Phi}^2}{2L}. \end{aligned} \tag{20}$$

2.3.3 Diagonalization of the core Hamiltonian

The core Hamiltonian may be divided into two sub-Hamiltonians H_I and H_R

$$\hat{H}_\mathrm{I} = \frac{\hat{Q}_\mathrm{N}^2}{2C_\mathrm{N}}, \tag{21}$$

$$\hat{H}_\mathrm{R} = \frac{(\hat{Q}+\alpha\hat{Q}_\mathrm{N})^2}{2C_\mathrm{R}} + \frac{\hat{\Phi}^2}{2L}, \tag{22}$$

corresponding to the energy of the QCR island and the resonator, respectively. The island Hamiltonian $\hat{H}_\mathrm{I}$ commutes with the island charge operator and thus shares its eigenstates. We define the eigenstates as $\hat{Q}_\mathrm{N}\left|q\right\rangle = eq\left|q\right\rangle$, where q is an integer. Furthermore, we define the charging energy of the island as $E_\mathrm{N} = \frac{e^2}{2C_\mathrm{N}}$. For the resonator Hamiltonian $\hat{H}_\mathrm{R}$, we label the eigenstates as $\left|m_q\right\rangle$, where m is positive integer and q refers to the island charge.

Let us next define another gauge transformation $\left|m\right\rangle = \mathrm{e}^{\frac{\mathrm{i}}{\hbar}\alpha q e\hat{\Phi}}\left|m_q\right\rangle$ to obtain the plain eigenstates of the resonator serving as a quantum harmonic oscillator (QHO). In this gauge, the core Hamiltonian becomes

$$\mathrm{e}^{\frac{\mathrm{i}}{\hbar}\alpha q e\hat{\Phi}}\hat{H}_0\mathrm{e}^{-\frac{\mathrm{i}}{\hbar}\alpha q e\hat{\Phi}} = \frac{\hat{Q}_\mathrm{N}^2}{2C_\mathrm{N}} + \frac{\hat{Q}^2}{2C_\mathrm{R}} + \frac{\hat{\Phi}^2}{2L} = \hat{H}_\mathrm{I} + \hat{H}_\mathrm{R}^{'}, \tag{23}$$

where $\hat{H}_\mathrm{R}^{'}$ is the cQED equivalent of the QHO Hamiltonian [39], and is therefore equal to $\hat{H}_\mathrm{R}^{'} = \hbar\omega_\mathrm{R}(\hat{a}^\dagger\hat{a}+\frac{1}{2})$, where $\omega_\mathrm{R} = (\sqrt{LC_\mathrm{R}})^{-1}$ is the angular frequency of the resonator, and $\hat{a}^\dagger$ and $\hat{a}$ are the bosonic creation and annihilation operators with Fock eigenstates $\left|m\right\rangle$. Thus, we can diagonalize the gauge transformed Hamiltonian in the product eigenstate basis $\left|q,m\right\rangle$ as

$$\mathrm{e}^{\frac{\mathrm{i}}{\hbar}\alpha q e\hat{\Phi}}\hat{H}_0\mathrm{e}^{-\frac{\mathrm{i}}{\hbar}\alpha q e\hat{\Phi}} = \sum_{q=-\infty}^{\infty}\sum_{m=0}^{\infty}\left|q,m\right\rangle\left\langle q,m\right|\left[E_\mathrm{N}q^2 + \hbar\omega_\mathrm{R}\left(m+\frac{1}{2}\right)\right], \tag{24}$$

from which we obtain the diagonalization of the original core Hamiltonian by transforming back to the original gauge and absorbing the unitary operators to the resonator states

$$\begin{aligned}\hat{H}_0 &= \sum_{q=-\infty}^{\infty}\sum_{m=0}^{\infty}\mathrm{e}^{-\frac{\mathrm{i}}{\hbar}\alpha q e\hat{\Phi}}\left|q,m\right\rangle\left\langle q,m\right|\mathrm{e}^{\frac{\mathrm{i}}{\hbar}\alpha q e\hat{\Phi}}\left[E_\mathrm{N}q^2 + \hbar\omega_\mathrm{R}\left(m+\frac{1}{2}\right)\right] \\ &= \sum_{q=-\infty}^{\infty}\sum_{m=0}^{\infty}\left|q,m_q\right\rangle\left\langle q,m_q\right|\left[E_\mathrm{N}q^2 + \hbar\omega_\mathrm{R}\left(m+\frac{1}{2}\right)\right].\end{aligned} \tag{25}$$

2.3.4 Microscopic Hamiltonian

The microscopic Hamiltonian, $\hat{H}_\mathrm{el} = \hat{H}_\mathrm{N} + \hat{H}_\mathrm{S} + \hat{H}_\mathrm{T}$, of the system describes the potential energy of the quasiparticles on each electrode and the quasiparticle tunneling between the quasiparticle energy levels of the electrodes. In the gauge of Eq. (20), the electrode Hamiltonians are given by the electron number for the normal electrode and the BCS mean-field description for the superconducting electrode as [20]

$$\hat{H}_{\mathrm{N}} = \sum_{l\sigma} \varepsilon_l \hat{d}^{\dagger}_{l\sigma}\hat{d}_{l\sigma}, \tag{26}$$

$$\hat{H}_{\mathrm{S}} = \sum_{k\sigma}(\epsilon_k - eV)\hat{c}^{\dagger}_{k\sigma}\hat{c}_{k\sigma} + \sum_{k}(\Delta_k \hat{c}^{\dagger}_{k\uparrow}\hat{c}^{\dagger}_{-k\downarrow} + \mathrm{H.c.}), \tag{27}$$

where $\hat{d}_{l\sigma}$ is the annihilation operator of spin-σ particle on state l at the normal electrode, $\hat{c}_{k\sigma}$ is the respective annihilation operator for the superconducting electrode, Δ_k is the gap parameter, and ε_l and ϵ_k are the quasiparticle energies on the normal-metal and superconducting electrode, respectively. The tunneling Hamiltonian is given by

$$\hat{H}_{\mathrm{T}} = \sum_{kl\sigma}(T_{lk}\hat{d}^{\dagger}_{l\sigma}\hat{c}_{k\sigma}\mathrm{e}^{-\frac{\mathrm{i}}{\hbar}e\hat{\Phi}_{\mathrm{N}}} + \mathrm{H.c.}), \tag{28}$$

where T_{lk} is the tunneling matrix element and the term $\exp(\pm\frac{\mathrm{i}}{\hbar}e\hat{\Phi}_{\mathrm{N}})$ induces a change $\pm e$ in the island charge, as seen from the eigenvalue of the transformed charge operator

$$\begin{aligned}\hat{Q}'_{\mathrm{N}}\left|q\right\rangle &= \mathrm{e}^{\mp\frac{\mathrm{i}}{\hbar}e\hat{\Phi}_{\mathrm{N}}}\hat{Q}_{\mathrm{N}}\mathrm{e}^{\pm\frac{\mathrm{i}}{\hbar}e\hat{\Phi}_{\mathrm{N}}}\left|q\right\rangle \\ &= (\hat{Q}_{\mathrm{N}} \pm e)\left|q\right\rangle \\ &= (eq \pm e)\left|q\right\rangle,\end{aligned} \tag{29}$$

due to the commutation relation $[\hat{\Phi}_{\mathrm{N}}, \hat{Q}_{\mathrm{N}}] = \mathrm{i}\hbar$.

In order to incorporate the effect of the bias voltage to the operators, we apply a time-dependent unitary transformation

$$\hat{U}_V(t) = \prod_{k\sigma}\mathrm{e}^{\frac{\mathrm{i}}{\hbar}eVt\hat{c}^{\dagger}_{k\sigma}\hat{c}_{k\sigma}}, \tag{30}$$

yielding a transformed total Hamiltonian [20]

$$\hat{H}' = \hat{U}^{\dagger}_V(\hat{H}_{\mathrm{el}} + \hat{H}_0)\hat{U}_V + \mathrm{i}\hbar(\partial_t\hat{U}^{\dagger}_V)\hat{U}_V. \tag{31}$$

Utilizing the anticommutation rules of the fermionic ladder operators $\hat{c}^{\dagger}_{k\sigma}$ and $\hat{c}_{k\sigma}$, we observe that the unitary transformation (31) acts only on the superconductor and tunneling Hamiltonians, leaving the normal-metal and core Hamiltonians intact. The transformed Hamiltonians $\hat{H}'_{\mathrm{S}}$ and $\hat{H}'_{\mathrm{T}}$ become

$$\hat{H}'_{\mathrm{S}} = \sum_{k\sigma}\epsilon_k\hat{c}^{\dagger}_{k\sigma}\hat{c}_{k\sigma} + \sum_k(\tilde{\Delta}_k\hat{c}^{\dagger}_{k\uparrow}\hat{c}^{\dagger}_{-k\downarrow} + \mathrm{H.c.}), \tag{32}$$

$$\hat{H}'_{\mathrm{T}} = \sum_{kl\sigma}(T_{lk}\hat{d}^{\dagger}_{l\sigma}\hat{c}_{k\sigma}\mathrm{e}^{-\frac{\mathrm{i}}{\hbar}e(\hat{\Phi}_{\mathrm{N}} - Vt)} + \mathrm{H.c.}), \tag{33}$$

where $\tilde{\Delta}_k = \Delta_k\mathrm{e}^{-\frac{2\mathrm{i}}{\hbar}eVt}$ is the transformed gap parameter independent of the density of states. Furthermore, we simplify the tunneling Hamiltonian into

$$\hat{H}'_{\mathrm{T}} = \hat{\Theta}\mathrm{e}^{-\frac{\mathrm{i}}{\hbar}e(\hat{\Phi}_{\mathrm{N}} - Vt)} + \mathrm{H.c.} \tag{34}$$

by defining the tunneling operator $\hat{\Theta} = \sum_{kl\sigma}T_{lk}\hat{d}^{\dagger}_{l\sigma}\hat{c}_{k\sigma}$.

2.3.5 Tunneling matrix elements

In order to derive the photon-number-dependent tunneling rates through the NIS junction, we need to solve the matrix elements $\langle f|\,\hat{H}_{\mathrm{T}}'\,|i\rangle$ appearing in the Fermi golden rule (1). The possible initial and final states of the system are the product states $|E, q, m_q\rangle$, where $|E\rangle$ is the product eigenstate of the electrode Hamiltonians (26) and (32). Thus, by applying Eq. (34), the tunneling matrix element can be written as

$$\begin{aligned}\langle f|\,\hat{H}_{\mathrm{T}}'\,|i\rangle = {} & \langle E', q', m'_{q'}|\,\hat{H}_{\mathrm{T}}'\,|E, q, m_q\rangle \\ = {} & \mathrm{e}^{\frac{\mathrm{i}}{\hbar}eVt}\,\langle E'|\,\hat{\Theta}\,|E\rangle\,\langle q', m'_{q'}|\,\mathrm{e}^{-\frac{\mathrm{i}}{\hbar}e\hat{\Phi}_{\mathrm{N}}}\,|q, m_q\rangle \\ & + \mathrm{e}^{-\frac{\mathrm{i}}{\hbar}eVt}\,\langle E'|\,\hat{\Theta}^{\dagger}\,|E\rangle\,\langle q', m'_{q'}|\,\mathrm{e}^{\frac{\mathrm{i}}{\hbar}e\hat{\Phi}_{\mathrm{N}}}\,|q, m_q\rangle\,.\end{aligned} \tag{35}$$

Since the flux operator $\hat{\Phi}_{\mathrm{N}}$ induces a charge shift e on the island charge, as shown in Eq. (29), all non-zero core matrix elements must satisfy

$$\begin{aligned}\langle q', m'_{q'}|\,\mathrm{e}^{\pm\frac{\mathrm{i}}{\hbar}e\hat{\Phi}_{\mathrm{N}}}\,|q, m_q\rangle &= \delta_{q',q\pm1}\,\langle m'_{q\pm1}|m_q\rangle \\ &= \delta_{q',q\pm1}\,\langle m'_{\pm1}|m_0\rangle \\ &= \delta_{q',q\pm1}\,\langle m'|\,\mathrm{e}^{\pm\frac{\mathrm{i}}{\hbar}\alpha e\hat{\Phi}}\,|m\rangle\,.\end{aligned} \tag{36}$$

Due to the Kronecker delta appearing in the matrix element above, the total matrix element is divided into two separate matrix elements corresponding to forward (N→S, $|q\rangle \rightarrow |q+1\rangle$) and backward tunneling (S→N, $|q\rangle \rightarrow |q-1\rangle$)

$$\langle f|\,\hat{H}_{\mathrm{T}}'\,|i\rangle_{\mathrm{N}\rightarrow\mathrm{S}} = \mathrm{e}^{-\frac{\mathrm{i}}{\hbar}eVt}\,\langle E'|\,\hat{\Theta}^{\dagger}\,|E\rangle\,\langle m'|\,\mathrm{e}^{\frac{\mathrm{i}}{\hbar}\alpha e\hat{\Phi}}\,|m\rangle\,, \tag{37}$$

$$\langle f|\,\hat{H}_{\mathrm{T}}'\,|i\rangle_{\mathrm{S}\rightarrow\mathrm{N}} = \mathrm{e}^{\frac{\mathrm{i}}{\hbar}eVt}\,\langle E'|\,\hat{\Theta}\,|E\rangle\,\langle m'|\,\mathrm{e}^{-\frac{\mathrm{i}}{\hbar}\alpha e\hat{\Phi}}\,|m\rangle\,, \tag{38}$$

and consequently, in the form of the Fermi golden rule (1) we obtain

$$\left|\langle f|\,\hat{H}_{\mathrm{T}}'\,|i\rangle\right|^2_{\mathrm{N}\rightarrow\mathrm{S}} = \left|\langle E'|\,\hat{\Theta}^{\dagger}\,|E\rangle\right|^2\left|\langle m'|\,\mathrm{e}^{\frac{\mathrm{i}}{\hbar}\alpha e\hat{\Phi}}\,|m\rangle\right|^2, \tag{39}$$

$$\left|\langle f|\,\hat{H}_{\mathrm{T}}'\,|i\rangle\right|^2_{\mathrm{S}\rightarrow\mathrm{N}} = \left|\langle E'|\,\hat{\Theta}\,|E\rangle\right|^2\left|\langle m'|\,\mathrm{e}^{-\frac{\mathrm{i}}{\hbar}\alpha e\hat{\Phi}}\,|m\rangle\right|^2. \tag{40}$$

Applying the definition of the resonator flux operator $\hat{\Phi} = \sqrt{\frac{\hbar}{2C_{\mathrm{R}}\omega_{\mathrm{R}}}}(\hat{a}^{\dagger} + \hat{a})$, we can write

$$\begin{aligned}\langle m'|\,\mathrm{e}^{\pm\frac{\mathrm{i}}{\hbar}\alpha e\hat{\Phi}}\,|m\rangle &= \langle m'|\,\mathrm{e}^{\pm\mathrm{i}\sqrt{\rho}(\hat{a}^{\dagger}+\hat{a})}\,|m\rangle \\ &= \langle m'|\,\hat{D}(\pm\mathrm{i}\sqrt{\rho})\,|m\rangle\,,\end{aligned} \tag{41}$$

where $\rho = \frac{\pi\alpha^2}{\omega_{\mathrm{R}}C_{\mathrm{R}}R_{\mathrm{K}}}$, $R_{\mathrm{K}} = \frac{2\pi\hbar}{e^2}$ is the von Klitzing constant, and $\hat{D}(\mu) = \mathrm{e}^{\mu\hat{a}^{\dagger}-\mu^*\hat{a}}$ is the displacement operator. Utilizing the displacement operator is convenient, since its matrix elements can be derived as [41]

$$\langle m'|\,\hat{D}(\mu)\,|m\rangle = \begin{cases} \mu^{l}\mathrm{e}^{-\frac{|\mu|^2}{2}}\left(\dfrac{m!}{m'!}\right)^{\frac{1}{2}} L_m^{(l)}(|\mu|^2), & m' \geq m, \\[2ex] (-\mu^*)^{-l}\mathrm{e}^{-\frac{|\mu|^2}{2}}\left(\dfrac{m'!}{m!}\right)^{\frac{1}{2}} L_{m'}^{(-l)}(|\mu|^2), & m' < m, \end{cases} \tag{42}$$

where $l = m' - m$ is an integer and $L_n^{(c)}(x)$ are the generalized Laguerre polynomials [42]. Consequently, the squared absolute value of the resonator matrix element becomes

$$\begin{aligned} M_{mm'}^2 &= \left|\langle m'|\, \mathrm{e}^{\pm \frac{\mathrm{i}}{\hbar}\alpha e\hat{\Phi}}\, |m\rangle\right|^2 \\ &= \rho^{|l|}\mathrm{e}^{-\rho}\left(\frac{m!}{m'!}\right)^{\mathrm{sqn}(l)}\left|L^{|l|}_{\min\{m,m'\}}(\rho)\right|^2 . \end{aligned} \tag{43}$$

2.3.6 Tunneling rates

Insertion of the matrix elements given by Eqs. (39) and (43) into the Fermi golden rule (1) yields the forward tunneling rate between the initial and final quasiparticle states $|E\rangle$ and $|E'\rangle$, respectively, associated with a photon number change $m \to m'$ in the resonator

$$\begin{aligned} \overrightarrow{\Gamma}^{E\to E'}_{q,m,m'}(V) =& \frac{2\pi M^2_{mm'}}{\hbar}\left|\langle E'|\, \hat{\Theta}^\dagger\, |E\rangle\right|^2 \\ &\times \delta[E_\mathrm{N}(2q+1) + \hbar\omega_\mathrm{R}(m'-m) + E' - E - eV], \end{aligned} \tag{44}$$

where E and E' are the energies of the initial and final quasiparticle states, respectively. Next, we consider a single term $T_{kl}\hat{c}^\dagger_{k\sigma}\hat{d}_{l\sigma}$ of the tunneling operator $\hat{\Theta}^\dagger$. For this single term, we observe that the matrix element $\langle E'|\, T_{kl}\hat{c}^\dagger_{k\sigma}\hat{d}_{l\sigma}\, |E\rangle$ is non-zero only if the initial and final states correspond to

$$\begin{cases} |E\rangle = |..., 1_{l\sigma}, ...\rangle_\mathrm{N}\, |..., 0_{k\sigma}, ...\rangle_\mathrm{S} \\ |E'\rangle = |..., 0_{l\sigma}, ...\rangle_\mathrm{N}\, |..., 1_{k\sigma}, ...\rangle_\mathrm{S}\, , \end{cases} \tag{45}$$

i.e., initially the state $|n_{l\sigma}\rangle_\mathrm{N}$ on the normal-metal electrode must be occupied and the state $|n_{k\sigma}\rangle_\mathrm{S}$ on the superconducting electrode must be unoccupied, while the occupation of any other state is arbitrary but identical between the initial and final states. Since in the tunneling event a single quasiparticle is transferred from the normal-metal electrode to the superconducting electrode, the occupation of the state $|n_{l\sigma}\rangle_\mathrm{N}$ decreases by one and the occupation of the state $|n_{k\sigma}\rangle_\mathrm{S}$ increases by one, and hence the total change in the quasiparticle energy is $E' - E = \epsilon_k - \varepsilon_l$. The probability of the initial state can be expressed using the Fermi function $f_j(E)$ as

$$p_E = f_\mathrm{N}(\varepsilon_l)\,[1 - f_\mathrm{S}(\epsilon_k)]\, . \tag{46}$$

Since the typical change in the quasiparticle energy during the tunneling event is small compared to the Fermi energy, we may assume that the tunneling matrix elements are approximately independent of energy. Consequently, by substituting $\sum_{kl\sigma}|T_{kl}|^2 = |T|^2$, integrating over all possible quasiparticle energies, and including the constant terms into the tunneling resistance R_T [34, 43], the total forward tunneling rate becomes

$$\begin{aligned} \overrightarrow{\Gamma}_{q,m,m'}(V) =& \frac{M^2_{mm'}}{e^2 R_\mathrm{T}}\int_{-\infty}^{\infty}\int_{-\infty}^{\infty} \mathrm{d}\varepsilon_l \mathrm{d}\epsilon_k n_\mathrm{S}(\epsilon_k) f_\mathrm{N}(\varepsilon_l)\,[1 - f_\mathrm{S}(\epsilon_k)] \\ &\times \delta[E_\mathrm{N}(2q+1) + \hbar\omega_\mathrm{R}(m'-m) + \epsilon_k - \varepsilon_l - eV] \\ =& M^2_{mm'}\frac{R_\mathrm{K}}{R_\mathrm{T}}\overrightarrow{F}(eV - \hbar\omega_\mathrm{R} l - E_q^+), \end{aligned} \tag{47}$$

where $E_q^{\pm} = E_{\mathrm{N}}(1 \pm 2q)$, and the normalized forward tunneling rate $\overrightarrow{F}(E)$ is given by

$$\overrightarrow{F}(E) = \frac{1}{h}\int_{-\infty}^{\infty} \mathrm{d}\varepsilon n_{\mathrm{S}}(\varepsilon) f_{\mathrm{N}}(\varepsilon - E)\left[1 - f_{\mathrm{S}}(\varepsilon)\right]. \tag{48}$$

Similar derivation can be applied for the backward tunneling rate, yielding

$$\overleftarrow{\Gamma}_{q,m,m'}(V) = M_{mm'}^2 \frac{R_{\mathrm{K}}}{R_{\mathrm{T}}} \overleftarrow{F}(eV + \hbar\omega_{\mathrm{R}} l + E_q^{-}), \tag{49}$$

where the normalized backward tunneling rate $\overleftarrow{F}(E)$ is given by

$$\overleftarrow{F}(E) = \frac{1}{h}\int_{-\infty}^{\infty} \mathrm{d}\varepsilon n_{\mathrm{S}}(\varepsilon) f_{\mathrm{S}}(\varepsilon)\left[1 - f_{\mathrm{N}}(\varepsilon - E)\right]. \tag{50}$$

2.3.7 Resonator transition rate

The tunneling rates derived above correspond to tunneling through an NIS junction. For the reverse configuration, the SIN rates corresponding to the core circuit transitions $|q, m_q\rangle \to |q+1, m_{q+1}\rangle$ and $|q, m_q\rangle \to |q-1, m_{q-1}\rangle$ are given by the rates (47) and (49), respectively, by simply switching the sign of the bias voltage $V \to -V$. Assuming the electrode temperatures are equal, we obtain a relation between the normalized forward and backward rates $\overrightarrow{F}(E) = \overleftarrow{F}(-E)$. Consequently, the total rate for both adding (+) or removing (−) a charge e from the normal-metal island via tunneling through the NIS junction can be rewritten from Eqs. (47) and (49) in terms of the normalized forward rate [20]

$$\Gamma_{q,m,m'}^{\pm}(V) = M_{mm'}^2 \frac{R_{\mathrm{K}}}{R_{\mathrm{T}}} \overrightarrow{F}(\pm eV - \hbar\omega_{\mathrm{R}} l - E_q^{\pm}). \tag{51}$$

In typical experimental conditions, elastic tunneling is the dominant transition process, allowing for a rapid thermalization of the island charge. Therefore, it is a valid assumption to consider the island charge and the resonator to be independent of each other, and write the charge-independent resonator transition rate as an average over the thermal charge distribution p_q [20]

$$\Gamma_{mm'}(V) = \sum_q p_q \left[\Gamma_{q,m,m'}^{+}(V) + \Gamma_{q,m,m'}^{-}(V)\right]. \tag{52}$$

Since the charging energy is typically small compared to other energy scales of the system, $E_{\mathrm{N}} \ll \Delta, \hbar\omega_{\mathrm{R}}, k_{\mathrm{B}}T$, we can expand Eq. (52) around $q = 0$, and note that the first and higher-order terms essentially vanish due to a factor $\frac{E_{\mathrm{N}}}{k_{\mathrm{B}}T} \ll 1$ [20, 44]. Therefore, only the charge-independent zeroth order term remains, and the resonator transition rate obtains the form

$$\Gamma_{mm'}(V) \approx M_{mm'}^2 \frac{R_{\mathrm{K}}}{R_{\mathrm{T}}} \sum_{\tau=\pm 1} \overrightarrow{F}(\tau eV - \hbar\omega_{\mathrm{R}} l - E_{\mathrm{N}}). \tag{53}$$

In the case of a symmetric double-junction QCR, the resulting transition rate is identical up to a constant factor 2 from the contribution of the other junction. For a single-junction QCR shunted to ground by a resonator, as used in the experiments of this thesis, a separate charge island does not exist. Therefore, we can further simplify the obtained resonator transition rate by considering the limit of large coupling capacitance and setting $E_\mathrm{N} = 0$, yielding

$$\Gamma_{mm'}(V) \approx M^2_{mm'} \frac{R_\mathrm{K}}{R_\mathrm{T}} \sum_{\tau=\pm 1} \overrightarrow{F}(\tau eV - \hbar\omega_\mathrm{R} l). \tag{54}$$

2.3.8 Characteristic parameters

Typically, the characteristic impedance of a coplanar waveguide resonator is much smaller than the von Klitzing resistance, $Z_\mathrm{R} \ll R_\mathrm{K}$. Therefore, the constant ρ in Eq. (43) is small, and we can approximate the resonator matrix elements in the lowest order of ρ as [20]

$$M^2_{mm'} \approx \frac{\rho^{|l|}}{|l|!} \binom{\max\{m, m'\}}{|l|}, \tag{55}$$

where $\binom{n}{k}$ is the binomial coefficient. Consequently, the matrix elements corresponding to transitions between the adjacent resonator states simplify into $M^2_{m,m+1} = \rho(m+1)$ and $M^2_{m,m-1} = \rho m$.

Essentially, photon-assisted tunneling can be considered as a route for decay or excitation of the resonator state coupled to a thermal reservoir. Using the lowest-order matrix elements derived above, we can define characteristic parameters for the reservoir by writing the single-photon transition rates as

$$\Gamma_{m,m+1} = \gamma_\mathrm{T} N_\mathrm{T} (m+1), \tag{56}$$

$$\Gamma_{m,m-1} = \gamma_\mathrm{T} (N_\mathrm{T}+1) m, \tag{57}$$

where γ_T is the coupling strength that describes the resonator decay induced by the QCR, $N_\mathrm{T} = \frac{1}{\exp[\hbar\omega_\mathrm{R}/(k_\mathrm{B}T_\mathrm{T})]-1}$ is the mean occupation of the bosonic reservoir, and T_T is the effective temperature of the reservoir. Comparing Eqs. (54), (56), and (57), we can write the characteristic parameters as

$$T_\mathrm{T} = \frac{\hbar\omega_\mathrm{R}}{k_\mathrm{B}} \left[\ln\left(\frac{\Gamma_{10}}{\Gamma_{01}}\right)\right]^{-1} = \frac{\hbar\omega_\mathrm{R}}{k_\mathrm{B}} \left[\ln\left(\frac{\sum_{\tau=\pm1} \overrightarrow{F}(\tau eV - \hbar\omega_\mathrm{R})}{\sum_{\tau=\pm1} \overrightarrow{F}(\tau eV + \hbar\omega_\mathrm{R})}\right)\right]^{-1}, \tag{58}$$

$$\gamma_\mathrm{T} = \Gamma_{10} - \Gamma_{01} = \frac{R_\mathrm{K}\rho}{R_\mathrm{T}} \sum_{l,\tau=\pm1} l\overrightarrow{F}(\tau eV - l\hbar\omega_\mathrm{R}). \tag{59}$$

For the single-junction QCR directly coupled to the resonator, we can take the limit of large coupling capacitance and use $\frac{C_\mathrm{c}}{C_\mathrm{N}} = 1$. Then, applying $\rho = \pi \frac{C_\mathrm{c}^2 Z_\mathrm{R}}{C_\mathrm{N}^2 R_\mathrm{K}}$ to Eq. (59), we obtain a simplified expression

$$\gamma_\mathrm{T} = \frac{4Z_0}{R_\mathrm{T}} \sum_{l,\tau=\pm1} l\overrightarrow{F}(\tau eV - l\hbar\omega_\mathrm{R}), \tag{60}$$

where $Z_0 = \frac{\pi}{4} Z_\mathrm{R}$ is the impedance of the coplanar waveguide, assuming that the considered resonator is a quarter-wave coplanar waveguide resonator.

2.4 Quantum Brownian refrigerator

A QCR that is activated by voltage fluctuations arising from its thermal environment can be construed as a Brownian refrigerator. Conceptually, a Brownian refrigerator utilizes random thermal fluctuations to extract heat from the system locally [18]. In the context of NIS junctions, thermal noise is conveniently produced by a coupled hot resistor, inducing a heat flow from the normal-metal lead to the superconductor, as proposed in Ref. [17].

In this thesis, we consider the cooling effect of the QCR on a resonator, mediated by the absorption of photons from the resonator. Thus, the relevant heat flow occurs between the resonator and the QCR. Assuming a hot resistor R_r is coupled to the QCR, with a negligible coupling to the resonator, the thermal voltage fluctuations generated in the resistor can be considered classically as a time-dependent auxiliary term in the total bias voltage seen by the QCR, following a similar treatment as used for an ac-powered QCR in Ref. [38]. Consequently, at a small dc bias voltage, quantum-circuit refrigeration can be activated if a sufficiently large voltage is produced by the thermal fluctuations in the resistor.

In the experiments of this thesis, we utilize an rf signal generator to produce the noise that drives the QCR. We can obtain a connection between the voltage fluctuations in the transmission line due to this artificial noise and the voltage fluctuations generated in a hot resistor by considering the approximately 50-Ω impedance of the transmission line as the coupled resistor. That is, we can determine an equivalent noise temperature for the critical noise power that is required to activate the refrigeration process. The root-mean-square voltage of the random thermal fluctuations of charge carriers in the resistor obeys Planck's blackbody radiation law [45]

$$V_\mathrm{r} = \sqrt{\frac{4hfBR_\mathrm{r}}{\mathrm{e}^{\frac{hf}{k_\mathrm{B}T_\mathrm{r}}} - 1}}, \tag{61}$$

where h is the normal Planck constant, f is the center frequency of the noise bandwidth B, and T_r is the temperature of the resistor. The root-mean-square voltage connects to the total noise power seen by the load as $P_\mathrm{r} = \frac{V_\mathrm{r}^2}{4R_\mathrm{r}}$. Applying this relation to Eq. (61), we can solve for the equivalent noise temperature

$$T_\mathrm{r} = \frac{hf}{k_\mathrm{B} \ln\left(\frac{1}{\bar{n}} + 1\right)}, \tag{62}$$

where $\bar{n} = \frac{P_\mathrm{r}}{hfB}$ is the mean number of thermal photons. For large photon numbers, as used in the experiments of this thesis, the above expression simplifies to the first order into

$$T_\mathrm{r} = \frac{P_\mathrm{r}}{k_\mathrm{B}B}. \tag{63}$$

In order to achieve a purely thermal drive, the activation temperature, i.e., the equivalent noise temperature of the critical artificial-noise power that activates the refrigeration, should be accessible in the operation regime of the QCR. That is, heating the resistor to the activation temperature should be achievable without significant heating of the quasiparticles, which could degrade the operation of the QCR. From the above expression (63), we find that the activation temperature can be reduced by increasing the noise bandwidth seen by the QCR or by elevating the system impedance to cut down the activation power.

2.5 Dispersive readout with a transmon qubit

In the experimental part of this thesis, we measure a sample that comprises a QCR coupled to a resonator, which is in turn coupled to a transmon qubit that is equipped with another resonator used for readout. Although the aim of the experiments is to observe the effect of the QCR on the resonator and not on the qubit, we can utilize the dispersive coupling between the resonators and the qubit for reading the resonator state.

The dispersive readout utilizing a single readout resonator coupled to a qubit is a typical method used in superconducting-qubit experiments [9]. In this case, the energy of the resonator-qubit system is typically described by the Jaynes–Cummings Hamiltonian [9, 39, 46]

$$\hat{H}_{\mathrm{JC}} = \hbar\omega_{\mathrm{RO}}(\hat{a}^\dagger\hat{a} + \frac{1}{2}) + \frac{\hbar\omega_{\mathrm{Q}}}{2}\hat{\sigma}_{\mathrm{z}} + \hbar g(\hat{\sigma}_+\hat{a} + \hat{\sigma}_-\hat{a}^\dagger), \tag{64}$$

where $\omega_{\mathrm{RO(Q)}}$ is the resonator (qubit) angular frequency, g is the coupling rate, $\hat{\sigma}_{\mathrm{z}} = |e\rangle\langle e| - |g\rangle\langle g|$ is the qubit phase flip operator, and $\hat{\sigma}_+ = |e\rangle\langle g|$ and $\hat{\sigma}_- = |g\rangle\langle e|$ are the raising and lowering operators of the qubit, respectively. In the dispersive regime $|\Delta_\omega| = |\omega_{\mathrm{Q}} - \omega_{\mathrm{RO}}| \gg g$, the frequency of the resonator is far-detuned from the qubit frequency, and the Jaynes-Cummings Hamiltonian simplifies into [9, 47]

$$\hat{H}_{\mathrm{d}} = \hbar(\omega_{\mathrm{RO}} + \chi\hat{\sigma}_{\mathrm{z}})(\hat{a}^\dagger\hat{a} + \frac{1}{2}) + \frac{\hbar}{2}(\omega_{\mathrm{Q}} + \chi)\hat{\sigma}_{\mathrm{z}}, \tag{65}$$

where $\chi = \frac{g^2}{\Delta_\omega}$ is the Lamb shift. The eigenstates of the dispersive Hamiltonian (65) are given by

$$|1n\rangle \approx -|e\rangle \otimes |n_{\mathrm{RO}}\rangle\,, \tag{66}$$

$$|2n\rangle \approx |g\rangle \otimes |n_{\mathrm{RO}} + 1\rangle\,, \tag{67}$$

where n_{RO} is the number of photons occupying the readout resonator. Thus, the eigenstates of the coupled system essentially correspond to the ground state and excited state of the qubit, with a fixed number of photons occupying the resonator. Consequently, we can interpret the dispersive Hamiltonian (65) such that the dispersive coupling induces a resonator frequency shift by $\pm\chi$, depending on the qubit state. Additionally, the qubit frequency acquires a Lamb shift arising from vacuum fluctuations of the electromagnetic field [48, 49].

Based on this dispersive coupling, the readout of the qubit is achieved by two-tone spectroscopy. With the qubit initially in the ground state $|g\rangle$, the readout resonator is driven at the lower resonance frequency $\omega_{\mathrm{RO}} - \chi$. Simultaneously, we apply a qubit drive, with which we perform a frequency sweep around the qubit frequency.

At $\omega_{\rm drive} = \omega_{\rm Q} + \chi$, the drive excites the qubit to the $|e\rangle$ state, and consequently the resonator frequency shifts by 2χ, resulting in a change in the amplitude and phase of the measured transmission or reflection signal applied to the resonator. Thus, the qubit frequency is observed as a peak or dip in the frequency spectrum, depending on the configuration.

The dispersive Hamiltonian can also be interpreted in an alternative way. By rearranging the terms, we can write

$$\hat{H}_{\rm d}^{\rm R} = \hbar\omega_{\rm R}(\hat{a}_{\rm R}^\dagger \hat{a}_{\rm R} + \frac{1}{2}) + \frac{\hbar}{2}(\omega_{\rm Q} + \chi_{\rm R} + 2\chi_{\rm R}\hat{n})\hat{\sigma}_{\rm z}, \tag{68}$$

where $2\chi_{\rm R}\hat{n} = \frac{2g_{\rm R}^2}{\omega_{\rm Q}-\omega_{\rm R}}\hat{a}_{\rm R}^\dagger \hat{a}_{\rm R}$ is the ac Stark shift. In this formulation, the dispersive coupling induces a total shift of $\chi_{\rm R} + 2n\chi_{\rm R}$ to the qubit frequency. Moreover, this shift depends on the occupation n of the resonator via the number operator $\hat{a}_{\rm R}^\dagger \hat{a}_{\rm R}$. Here, we consider another resonator, which we label the reset resonator, coupled to the qubit that is also coupled to a readout resonator, similarly to the device presented in Sec. 3.1, see Figs. 3 and 6. The formulation of Eq. (68) is meaningful in the case where the linewidths of the qubit and the reset resonator are small compared to the dispersive shift $\chi_{\rm R}$. In this case, the occupation on the reset resonator induces a dispersive shift to the qubit frequency, which we can observe in a two-tone spectroscopy introduced above, as a shift of the qubit resonance peak on the frequency spectrum.

Under typical experimental conditions, the reset resonator has a thermal population of photons, i.e., the number of photons is not constant, but instead the resonator state is a weighted combination of all Fock states

$$\hat{\rho} = \sum_n p_{\rm thermal}(n)\,|n\rangle\langle n|\,. \tag{69}$$

The mean photon number follows the Bose-Einstein distribution [46]

$$\bar{n} = \frac{1}{{\rm e}^{\hbar\omega_{\rm R}/(k_{\rm B}T)} - 1}, \tag{70}$$

where $k_{\rm B}$ is the Boltzmann constant and T is temperature. The probability of occupation n on the mode is obtained as the probability of the respective microstate in the canonical ensemble

$$p(n) = \frac{1}{Z}{\rm e}^{-\beta E_n}, \tag{71}$$

where $Z = \sum_n {\rm e}^{-\beta E_n}$ is the partition function, $\beta = \frac{1}{k_{\rm B}T}$, and E_n is the energy of state $|n\rangle$. Inserting $E_n = n\hbar\omega_{\rm R}$ and applying Eq. (70), the probability can be expressed using the mean photon number $\bar{n}$ of the mode as [46]

$$p_{\rm thermal}(n) = \frac{\bar{n}^n}{(1+\bar{n})^{n+1}}. \tag{72}$$

From Eq. (72) we observe that for a thermal population, the $|0\rangle$ state always has the highest probability, and while the few-photon states $n = 1, 2$ can still have a significant probability for $\bar{n} \sim 1$, the probability of larger photon numbers vanishes quickly.

Similarly, the resonator can be driven with a microwave signal at the resonance frequency, in the case of which the resonator adopts a coherent state [46]

$$|\alpha\rangle = \mathrm{e}^{-\frac{|\alpha|^2}{2}} \sum_n \frac{\alpha^n}{\sqrt{n!}} |n\rangle \,, \tag{73}$$

that corresponds to Poisson distribution of probabilities

$$p_{\text{coherent}}(n) = \mathrm{e}^{-\bar{n}} \frac{\bar{n}^n}{n!}. \tag{74}$$

Since in both cases above the resonator state is a combination of all Fock states, when coupled to a qubit in the dispersive limit, the resonator induces an ac Stark shift $2n\chi_{\mathrm{R}}$ to the qubit frequency for each n. As a result, the qubit excitation frequency splits into multiple $2\chi_{\mathrm{R}}$-spaced frequencies that each correspond to a different Fock state $|n\rangle$. If the coupling to the qubit is sufficiently strong, such that the dispersive shift exceeds the linewidth of the qubit resonance peak, the splitted frequencies can be resolved in a two-tone spectroscopy as separate peaks [50]. Since the probability of occupation n links directly to the qubit excitation at the corresponding frequency, the probability distribution of the Fock states is visible as a relative amplitude distribution of the measured qubit resonance peaks.

Here, we note that the extraction of photon statistics from the qubit spectrum is not flawless, since the linewidth of the qubit resonance peaks increases with photon number, and hence the higher photon number peaks become flattened [50]. For this reason, the highest photon number peaks are unresolvable even if the value of $\bar{n}$ increases. Furthermore, the two-tone spectroscopy approach may lead to complex dynamics that slightly alter the photon number distribution from the initial thermal state [50]. However, for the purpose of this thesis, the dispersive approach provides sufficiently accurate photon statistics for observing the decrease in the mean photon number of the resonator coupled to a QCR.

Utilizing the discussed two-way dispersive coupling for the readout, we can observe the operation of the QCR in a straightforward manner. As the QCR absorbs photons from the reset resonator, the mean photon number of the resonator decreases, which appears as a decreasing or vanishing amplitude of the higher photon number peaks, whereas the amplitude of the $|0\rangle$-state peak increases.

3 Sample layout and fabrication

This chapter provides an overview of the sample studied in the experiments of this thesis. The sample structure and layout is presented in Sec. 3.1, and the fabrication process is discussed in Sec. 3.2.

3.1 Sample structure

The sample studied in this thesis comprises a single-junction QCR in a direct contact with a quarter-wave coplanar waveguide (CPW) resonator, which we label the reset resonator. The layout of the sample is presented in Fig. 3. The reset resonator couples capacitively to a transmon qubit, the frequency of which can be tuned by applying a bias voltage to a flux line that induces a magnetic field through a superconducting quantum interference device (SQUID). The qubit is further coupled to a readout resonator, which capacitively couples to a transmission line used for the readout signal. The CPW transmission lines are designed for 50 Ω characteristic impedance.

The cross-section of the device is shown in Fig. 4. The sample is fabricated on a six-inch intrinsic-silicon wafer. The material of the ground plane and the resonator structures is niobium, which is superconducting at the measurement temperature. The superconducting electrodes of the Josephson junctions (SIS) that define the SQUID structure are made of aluminum, the main advantages of which include the availability, a relatively low melting point enabling growth by evaporation, and the natural formation of a native surface oxide film that acts as a tunnel junction barrier. Aluminum is used also for the superconducting electrode of the NIS junction, whereas

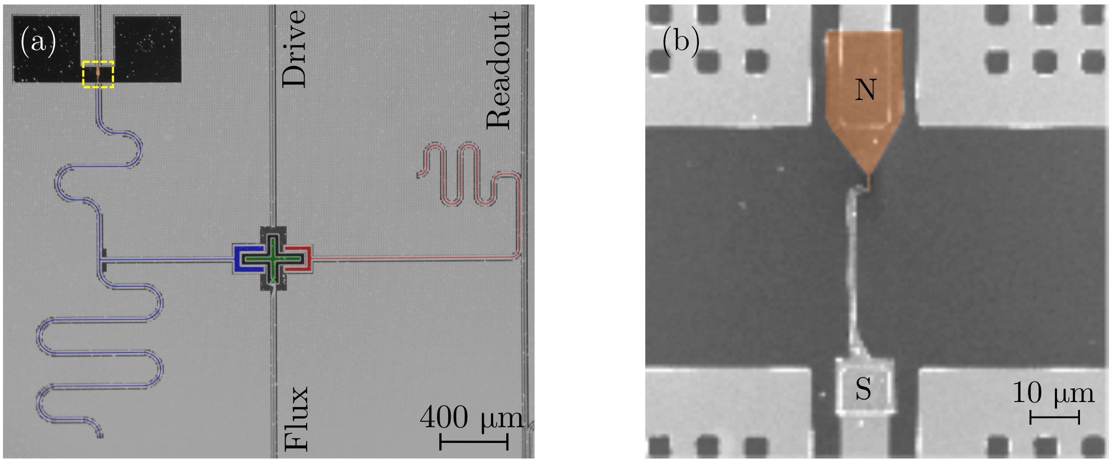

Figure 3: (a) False-color optical microscope image of a representative sample. The readout and reset resonators are highlighted by red and blue, respectively, and the QCR and the qubit are denoted by orange and green, respectively. (b) Close-up scanning electron microscope image of a single-junction QCR of a similar sample. Here, the orange-colored normal-metal electrode (N) overlaps with the oxidized long superconducting electrode (S) to vertically form the NIS tunnel junction.

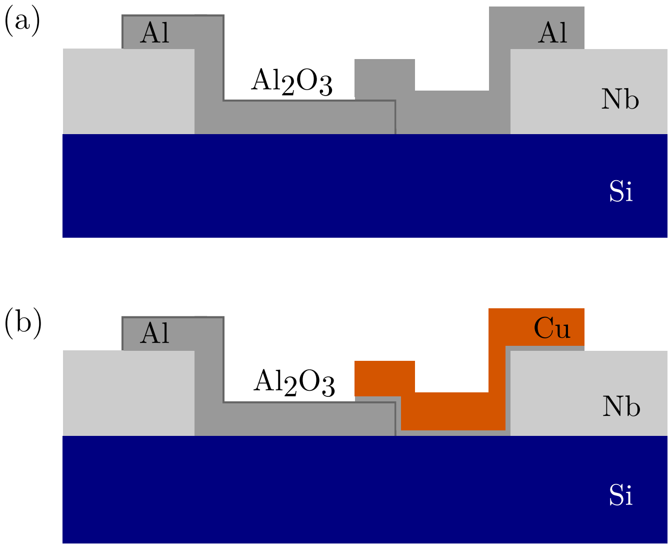

Figure 4: Off-scale schematic cross-section of the junction area for (a) SIS junction (b) NIS junction. A thin aluminum layer is evaporated below the copper electrode for the NIS junction to enhance the adhesion.

copper is used for the normal-metal electrode. Compared with other low-temperature normal-conductors, copper has a very high electric and thermal conductivity, and it adheres more strongly to silicon substrates than the other typical high-conducting materials gold and silver.

3.2 Fabrication process

The ground plane and the resonators are created by sputtering a 200-nm film of niobium on top of the silicon wafer, and defining the structures using optical lithography and plasma etching. Next, the SIS junctions and the NIS junction are deposited in two respective lithography steps.

The tunnel junction lithography process is illustrated in Fig. 5. First, we spin coat the wafer with roughly 700 nm of copolymer methyl methacrylate (MMA) and 200 nm of poly(methyl methacrylate) (PMMA), to form a bilayer resist stack. The junction area is then defined by electron-beam lithography (EBL), in which a high-energy electron beam exposes the desired pattern on the resist, making the resist soluble in a developer in these regions. After exposing the electrode structure, we apply a small extra dose over the whole junction area, in order to form an undercut to the copolymer layer. Since the copolymer resist is more sensitive to electrons than the top PMMA layer, this small dose does not ideally affect the pattern on the top layer, but only clears the bottom layer in that area.

After the EBL, the resist pattern is developed by consecutively submerging the sample in methyl-isobutyl-ketone:isopropanol (MIBK:IPA) (1:3), methylglycol:methanol (1:2), and isopropanol (IPA), for 20 seconds in each. Mainly, the top PMMA layer dissolves in the MIBK:IPA solution, whereas the purpose of methylglycol:methanol is to enhance the undercut. Since the MIBK:IPA solution also dissolves the copolymer MMA, the development process can alternatively be performed by a single soak in MIBK:IPA for a slightly longer time, followed by a rinse in pure IPA

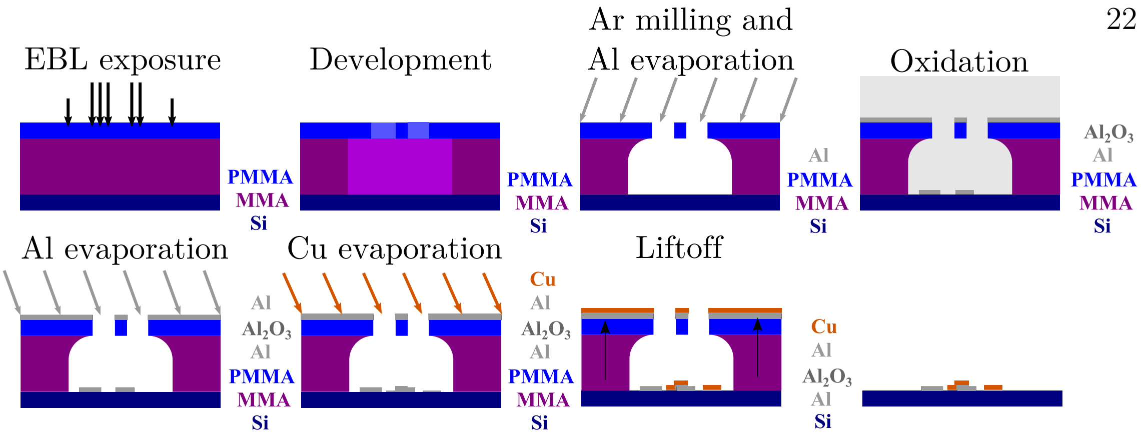

Figure 5: Off-scale schematic illustration of the tunnel junction lithography process for NIS junctions. The process is similar for SIS junctions, except that the second evaporation step after the oxidation only includes the deposition of aluminum.

to interrupt the development.

The junctions are fabricated by physical vapor deposition (PVD) in an electron-beam evaporator. The electron beam heats up the metallic target material inside a vacuum chamber, emanating vaporized material particles that enter through the holes in the resist, defined in the EBL step, and solidify on top of the substrate surface. Since a native oxide layer forms on the surface of the niobium structures when exposed to air, we use argon milling on the sample, prior to the evaporation. In this process, the oxide layer is removed by a beam of high-energy argon ions, which enhances the electric contact between the junction electrodes and the niobium leads.

In order to create the SIS or NIS structure, we utilize a two-angle Dolan shadow evaporation technique. After the EBL exposure, development, and argon cleaning steps, here we first tilt the sample to a 20° angle with respect to the direction of the incident particles. Due to the bilayer resist structure with an undercut, the vapor hits the substrate at a position, which is slightly shifted in x direction, with respect to normal incidence. At this tilt angle, we deposit a 30-nm layer of aluminum to create the first electrode. Next, we let oxygen into the deposition chamber, to reach an oxidation pressure in the few-millibar range, and let the sample sit for at least five minutes, to allow the thin native oxide layer to form on the aluminum surface.

After pumping the oxygen out of the chamber, we tilt the sample to a $-20°$ angle and deposit the second electrode. At this angle, the pattern shifts in the opposite direction compared to the first deposition. Thus, the junction is formed in vertical direction by two overlapping fingers with an insulating oxide in between. For the SIS junctions of the SQUID, we evaporate 30 nm of aluminum for the second electrode. For the NIS junction, we first evaporate 3 nm of aluminum, and then 60 nm of copper at the second tilt angle to create the normal-metal electrode. The purpose of the thin aluminum layer below the copper layer is to enhance the contact to the aluminum oxide layer. Since the aluminum film is very thin, it remains normal-conducting, due to the inverse proximity effect [24].

After the deposition process, the sample is submerged in acetone for overnight, to lift off the remaining resist and the extra metal deposited on top of it. After rinsing with IPA and drying with N_2, the sample is wirebonded to a printed circuit board (PCB) which is integrated to a gold sample holder.

4 Experimental methods

In this chapter, we discuss the experimental methods used in this thesis. The experimental setup is presented in Sec. 4.1, and the measurement protocols are covered in Sec. 4.2.

4.1 Measurement setup

The experimental setup is illustrated in Fig. 6. The sample is installed in a dilution refrigerator, which reaches a temperature of 35 mK during the measurements, well below the superconducting transition temperature of both niobium (9 K) and aluminum (1.2 K) bulk. The filtering and attenuation configurations of the different input lines of the sample are collected in Table 1.

The setup comprises four rf drives: readout (RO) drive, qubit drive, reset drive, and QCR drive (SG396). The readout drive consists of an rf-signal source combined with an arbitrary-waveform generator (AWG) through an in-phase–quadrature-phase (IQ) mixer. The attenuation of the readout signal can be tuned by a room temperature digital attenuator, which also adds an insertion loss of 8.5 dB at the readout frequency. The signal is further attenuated and filtered at cryogenic temperatures inside the dilution refrigerator (see Table 1), and guided to the readout transmission line in the sample. The signal reflected from the readout resonator is amplified with a traveling-wave parametric amplifier (TWPA) and measured at the readout card, which compares the output signal with the input signal.

The reset resonator is driven from the qubit side, utilizing the qubit driveline. In principle, the reset resonator could also be driven from the QCR driveline, however, in this setup, the low-pass filter on the QCR side with a 3.4-GHz cutoff frequency strongly attenuates the drive signal at the resonator frequency, which would require a very large driving power. At room temperature, the attenuation of both the reset

Table 1: Filtering and attenuation of the input lines of the sample. Cryo refers to filters and attenuators placed inside the dilution refrigerator, and RT refers to those outside the refrigerator at room temperature. In the filter model name, VLF(X)- and BLP-types are low-pass filters, and VHF refers to a high-pass filter. The number in the model name roughly corresponds to the cutoff frequency of the filter in MHz.

		QCR dc	**QCR rf**	**Flux dc**
Filter	**Cryo**	VLFX-80+	VLF-3400+	–
	RT	2×BLP-1.9+	–	BLP-1.9+
Attenuation	**Cryo**	–	-60 dB	–
	RT	–	–	1 kΩ resistor

		Qubit drive	**Reset drive**	**RO drive**
Filter	**Cryo**	VHF-5500+		VHF-4400+
	RT	–		–
Attenuation	**Cryo**	-40 dB + -20 dB dir.coupl.		-80 dB
	RT	Digital att. + -10.3 dB		Digital att. + -8.5 dB

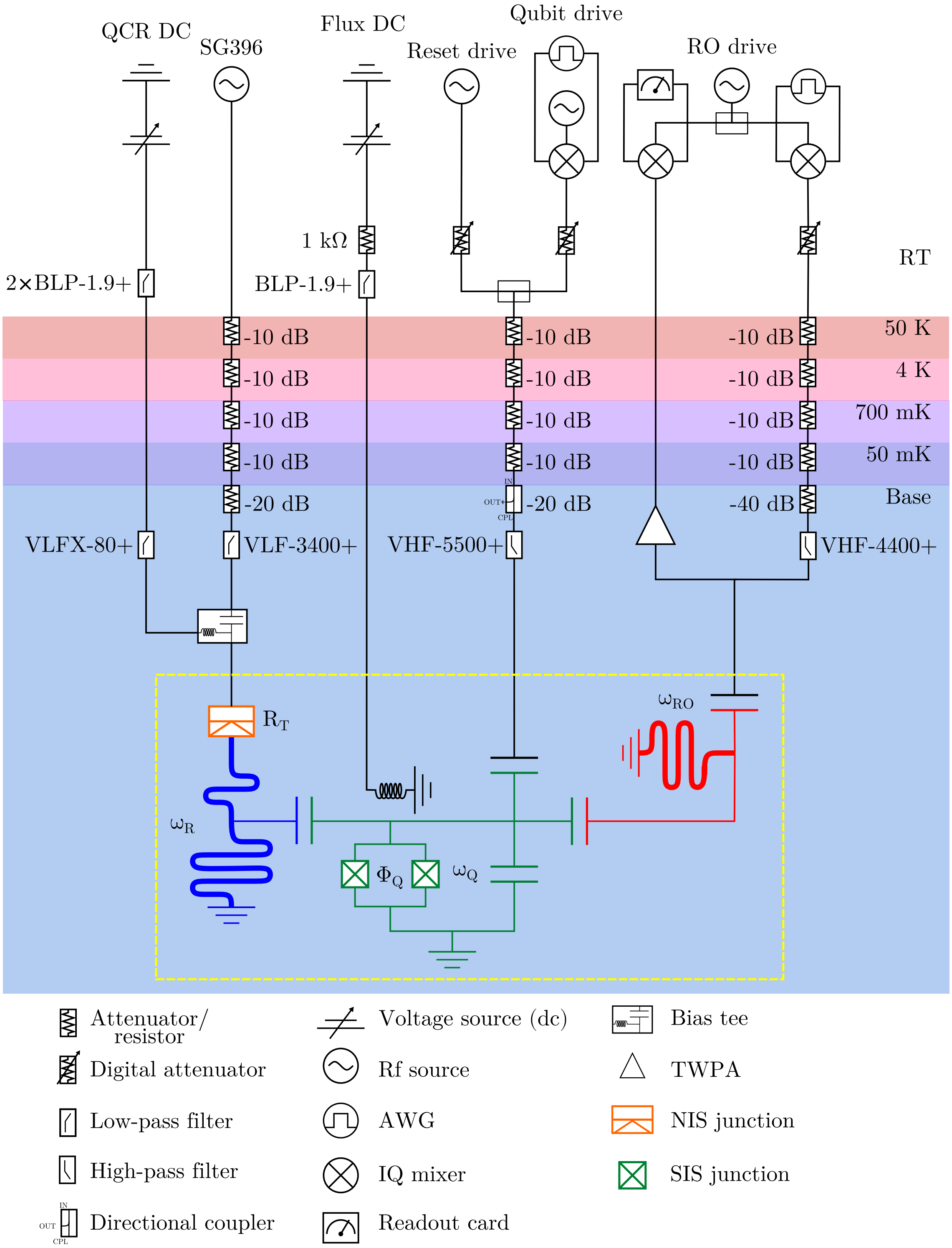
QCR DC
SG396
Flux DC
Reset drive
Qubit drive
RO drive
1 kΩ
2×BLP-1.9+
BLP-1.9+
RT
-10 dB
50 K
4 K
700 mK
50 mK
Base
-20 dB
-40 dB
IN
OUT
CPL
VLFX-80+
VLF-3400+
VHF-5500+
VHF-4400+
R_T
ω_RO
ω_R
Φ_Q
ω_Q
Attenuator/ resistor
Digital attenuator
Low-pass filter
High-pass filter
Directional coupler
Voltage source (dc)
Rf source
AWG
IQ mixer
Readout card
Bias tee
TWPA
NIS junction
SIS junction

Figure 6: Schematic illustration of the experimental setup. The temperature stages of the dilution refrigerator are highlighted with different colors. The components residing on the sample according to Fig. 3 are within the region denoted by the yellow dashed line. The model names that are given next to the filter symbols are specified in the caption of Table 1.

drive signal and the qubit drive signal are modified with the digital attenuator. At the operation frequency of the qubit and the reset resonator, the insertion loss of the digital attenuator is approximately 7 dB. After the digital attenuator, the reset and qubit drivelines are combined to a single driveline using a splitter. The insertion loss of the splitter is 3.3 dB at the relevant operation frequencies. The combined drive signal is further attenuated and filtered at cryogenic temperatures.

The QCR driveline is filtered and attenuated at the cryogenic temperatures. We use the noise generated by SRS SG396-model signal generator to drive the QCR. The QCR is also connected through a cryogenic bias tee to a Keithley 6430 source-measure unit (SMU) that acts as a dc bias-voltage source, and also enables measuring the current through the NIS junction.

The resonance frequency of the qubit is tuned with the SQUID by applying a dc bias voltage to the flux line. Since the flux line is a plain coplanar waveguide connected to ground at the other end, a 1-kΩ resistor is inserted between the voltage source and the flux line input at room temperature to restrict the current.

In Sec. 5, we use the terms *drive power* and *noise power* to express the input power from the microwave or noise source, entering the system after the possible digitally controlled attenuation, excluding the insertion loss of the digital attenuator and any further attenuation from cryogenic attenuators and filters that is listed in Table 1.

4.2 Measurement protocol

The primary measurement protocols used to characterize the sample include current-voltage (IV) measurements and two-tone spectroscopy. In IV measurements, we utilize the SMU connected to the QCR to simply sweep over a range of voltages, while measuring the tunneling current passing through the junction. Due to the superconducting gap involved in the tunneling process, as discussed in Sec. 2.1, we observe a low-current plateau in the obtained IV curve, around zero bias voltage. When the bias voltage is increased beyond the superconductor gap, current through the junction increases as a function of bias voltage, eventually reaching an ohmic dependence well above the gap.

Multiple characteristic parameters can be extracted from the IV curve. A quick estimate for the tunneling resistance R_T can be obtained by fitting the resistance given by Ohm's law in the ohmic regime above the gap. By comparing the resistances in the subgap and ohmic regimes, we can extract the Dynes parameter η expressing the smearing of the IV curve. The relation between the subgap current and voltage is obtained by linearizing the expression for the elastic tunneling current through the junction as [51]

$$I_\mathrm{sub}(V) \simeq \sqrt{\frac{\eta^2}{\eta^2+1}}\frac{V}{R_\mathrm{T}}. \tag{75}$$

In the usual experimental conditions, the Dynes parameter is small, $\eta \ll 1$, in which case we can solve for the Dynes parameter from the simple relation

$$\eta \simeq \frac{R_\mathrm{T}}{R_\mathrm{sub}}, \tag{76}$$

where $R_{\mathrm{sub}} = \frac{V}{I_{\mathrm{sub}}}$ is the subgap resistance given by the fit of Ohm's law in the subgap regime.

To obtain more detailed characteristics of the NIS junction, we can utilize Eq. (2) to extract an expression for the tunneling current as a function of bias voltage. In the characterization measurements, we assume that the PAT processes are negligible in the absence of driving applied to the resonators and the qubit. Thus, assuming only elastic tunneling, $P(E - E') = \delta(E - E')$, and using the definition of tunneling current $I_{1\to 2}(V) \equiv -e \left[\overrightarrow{\Gamma}_{1\to 2}(V) - \overrightarrow{\Gamma}_{2\to 1}(-V)\right]$, we obtain

$$I(V) = \frac{1}{eR_{\mathrm{T}}} \int_{-\infty}^{\infty} \mathrm{d}\varepsilon n_{\mathrm{S}}(\varepsilon - eV) \left[f(\varepsilon - eV) - f(\varepsilon)\right]. \tag{77}$$

By fitting Eq. (77) to the data of an IV measurement and utilizing Eq. (3) and the definition of the Fermi function $f(E) = \frac{1}{\exp[E/(k_{\mathrm{B}}T_{\mathrm{el}})]+1}$, we obtain estimates for the tunneling resistance R_{T}, Dynes parameter η, gap parameter Δ, and the electron temperature of the electrodes $T_{\mathrm{el}} = T_{\mathrm{N}} = T_{\mathrm{S}}$ as the fit parameters. In practice, the integration limits at infinity are replaced by a much smaller cutoff energy, since for large arguments, the two Fermi functions in Eq. (77) approach each other, and thus the contribution of high-energy states is negligible.

To characterize the two resonators and the qubit, we utilize the two-tone spectroscopy. In this method, we drive and measure the signal reflected from the readout resonator near its resonance frequency, while using another tone to sweep over the qubit or reset resonator frequency. When the second tone reaches the resonance frequency, the readout frequency shifts slightly, due to the dispersive coupling discussed in Sec. 2.5, which results in a change in the measured amplitude and phase of the readout signal. Depending on the sensing point used for probing the readout resonator, either a dip or a peak can be observed in the frequency spectrum of the second tone.

The effect of various tunable parameters on the resonance dips or peaks can be investigated by combining a sweep of the parameter to the two-tone measurement. The result of this 2D sweep can be visualized as a color map, presenting the probe frequency on the y-axis and the parameter on the x-axis, with the color scale expressing the phase or amplitude of the readout signal. From this 2D-sweep spectrum, we can search for a sweet spot of the parameter that enables optimal sensing of the state of the reset resonator. By driving both resonators and sweeping over the qubit frequency, we can observe the splitting of the qubit resonance into evenly spaced Fock spectral lines, the amplitude distribution of which approximately corresponds to the photon-number distribution of the quantum state of the reset resonator.

To obtain a strong response in the readout amplitude or phase signal from the dispersive shift, the sensing point, i.e., the drive frequency of the readout resonator is chosen to be roughly at the half-maximum point of the resonance peak. The two-tone spectra are averaged over a large number (typically 10000–80000) of traces to reduce the noise level in the images. To further enhance the clarity of the 2D-sweep spectra, we subtract from the data the average background response of the system to the sweep of the x-axis parameter.

5 Results

Here, we present and discuss the experimental results obtained for the QCR sample and setup introduced in Secs. 3 and 4. Section 5.1 presents the results of various characterization measurements that yield useful information about the operation of the device and the effect of the experimental parameters. In Sec. 5.2, we study the quality of analog frequency-modulated (AFM) noise generated by the SG396 signal generator by applying it as a drive for the reset resonator and measuring the power spectral density of the noise. Next, we apply the AFM noise to the QCR to induce damping of a coherent state of the reset resonator in Sec. 5.3, in close resemblance with the operation principle of the QBR. Finally, in Sec. 5.4, we explore another noise type generated by SG396, namely vector frequency modulation (VFM), and its properties as a drive for the reset resonator and the QCR.

5.1 Characterization of the device

The relevant characteristic parameters of the sample are collected into Table 2. The characterization of the sample starts by searching for the offset bias of the QCR. If the offset is large, the QCR can pass current even when biased at 0 V. Thus, to ensure that the QCR is not operating and interfering with the other characterization measurements, we find and set the offset bias voltage to keep the QCR in the off state. Figure 7 shows an IV measurement of the NIS junction. Here, we obtain a voltage offset of -1.12 mV from the midpoint of the low-current plateau. A quick estimate of the tunneling resistance of the junction is obtained from the slope of a linear fit to the curve in the ohmic regime above the gap for both positive and negative biases. The average tunneling resistance from the two fits shown in Fig. 7 is thus $R_\mathrm{T} = 22.1$ kΩ. Inserting this value of tunneling resistance and the subgap resistance $R_\mathrm{sub} = 5.95$ MΩ, obtained from another fit in the subgap regime into Eq. (76), yields a Dynes parameter of $\eta = 3.7 \times 10^{-3}$.

A more detailed characterization of the NIS junction can be obtained by fitting the current–voltage relation of Eq. (77) to the data in Fig. 7. From the fit parameters, we obtain slightly different values for the tunneling resistance $R_\mathrm{T} = 29.4$ kΩ and

Table 2: Summary of the system parameters extracted from the characterization measurements. R_T is the tunneling resistance of the NIS junction, η is the Dynes parameter, Δ is the gap parameter of the superconductor, T_el is the electron temperature of the normal-metal and superconducting electrodes, f_RO, f_R, and f_Q are the resonance frequencies of the readout resonator, reset resonator and the qubit, respectively, and χ_R is the dispersive shift due to the coupling between the qubit and the reset resonator.

R_T	η	Δ	T_el
29.4 kΩ	5.0×10^{-3}	203 μeV	248 mK

f_RO	f_R	f_Q	$\chi_\mathrm{R}/(2\pi)$
7.437 GHz	4.671 GHz	3.953 GHz	-2.2 MHz

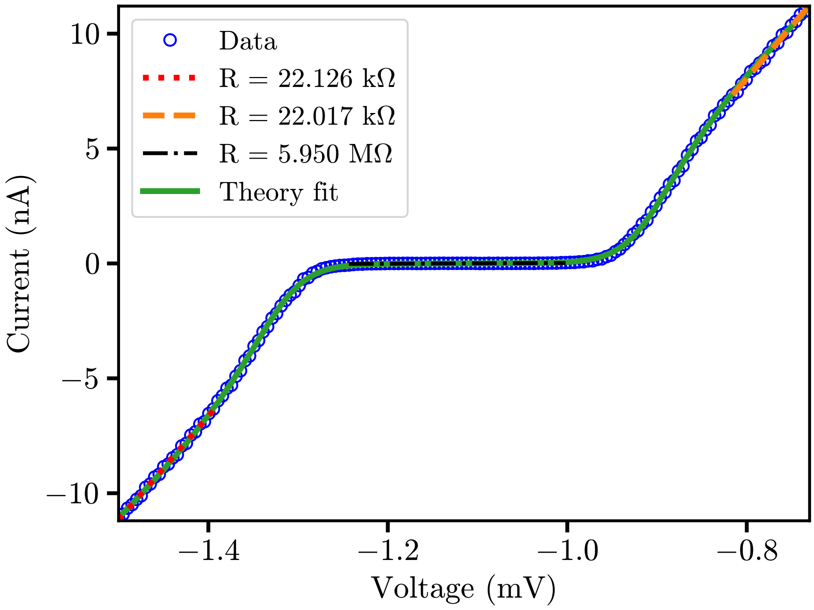

Figure 7: Current through the NIS junction as a function of voltage (blue circles), averaged over 10 measurements. The voltage offset obtained from this plot is −1.12 mV. The linear estimate of the tunneling resistance of the junction is obtained as the average of the two fits far from the current plateau, denoted by the red dotted line and orange dashed line. The subgap resistance used for calculating the Dynes parameter is obtained from the fit denoted by black dash-dotted line. More detailed characteristics are obtained from the theoretical fit (green solid line) of Eq. (77), from which we obtain $T_{\mathrm{el}} = 248$ mK, $\Delta = 203\ \mu$eV, $\eta = 1.96 \times 10^{-3}$, and $R_{\mathrm{T}} = 29.4$ kΩ as the fit parameters.

the Dynes parameter $\eta = 2.0 \times 10^{-3}$. This value of tunneling resistance is likely more accurate compared to the one obtained from the linear fit, since the measured voltages are still relatively close to the gap region, and thus the ohmic approximation is not completely valid. Based on qualitative observations on the fitting procedure, the Dynes parameter seems to be rather sensitive to the approximations made in the numerical calculations, such as the density of integration points and the choice of integration limits. Furthermore, for the tunneling resistance $R_{\mathrm{T}} = 29.4$ kΩ from Eq. (76), we would expect the Dynes parameter to be greater than that from the linear fit. Thus, to obtain a more reasonable estimate for the Dynes parameter, we insert the refined resistance value to Eq. (76), yielding $\eta = \frac{29.4\ \mathrm{k}\Omega}{5.95\ \mathrm{M}\Omega} \approx 5.0 \times 10^{-3}$. From the fit parameters, we also obtain the gap parameter $\Delta = 203\ \mu$eV and the electron temperature on the two leads $T_{\mathrm{el}} = 248$ mK, assuming equal thermalization.

During other characterization measurements, in which the effect of the QCR is not examined, we apply the offset voltage found from the IV curve to the QCR to set it to the off state. Figure 8 shows the effect of the flux bias voltage on the resonance frequencies of the system. Primarily, the flux bias tunes the qubit excitation frequency by inducing an external flux through the SQUID. Since the qubit is dispersively

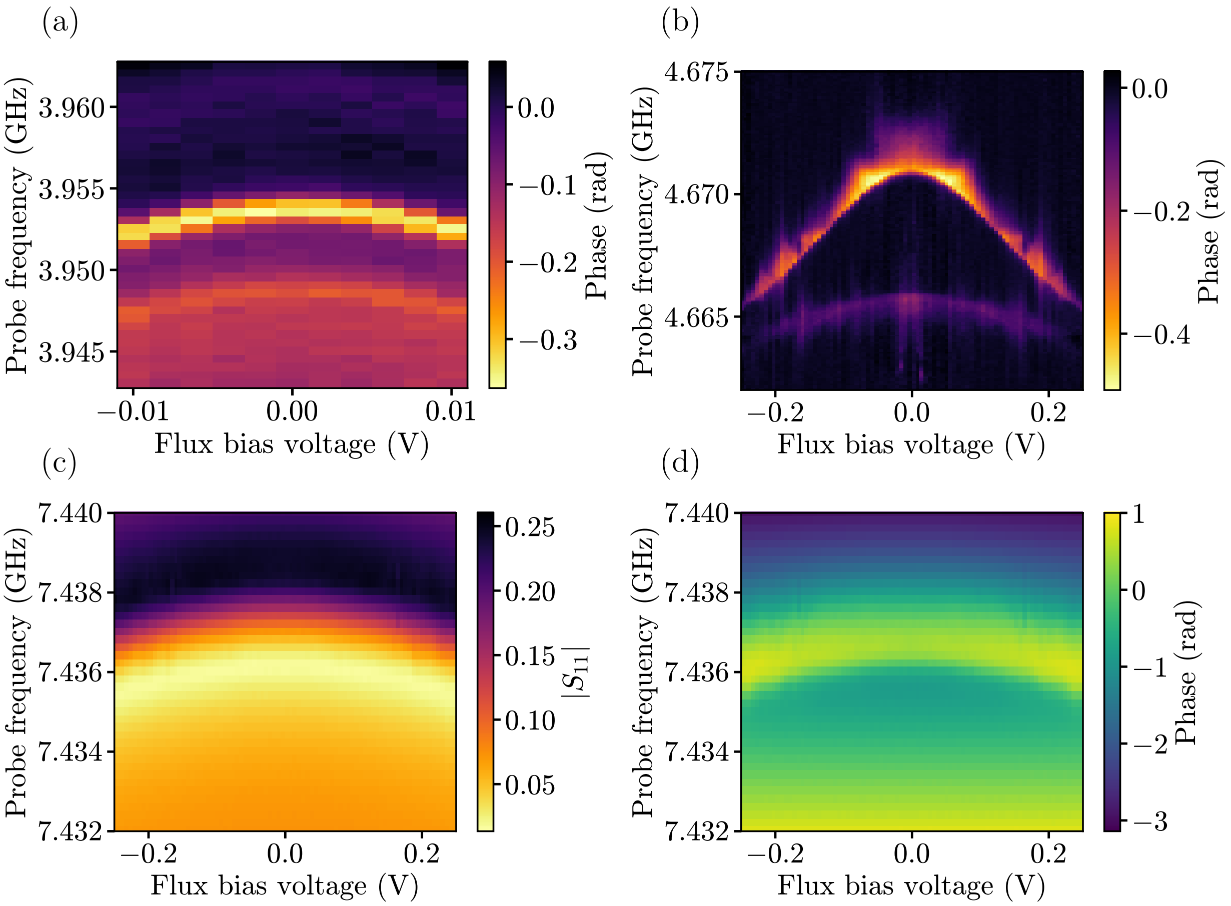

Figure 8: Readout response as a function of flux bias voltage and probe frequency swept near the resonance frequencies of the (a) qubit, (b) reset resonator, and (c),(d) readout resonator. In (a), (b), and (d), the phase of the readout signal is shown, whereas (c) presents the measured reflection amplitude from the readout resonator. The characteristic frequencies extracted here are $f_{\mathrm{RO}} = 7.437$ GHz, $f_{\mathrm{Q}} = 3.953$ GHz, and $f_{\mathrm{R}} = 4.671$ GHz, for the readout resonator, qubit, and reset resonator, respectively.

coupled to the two resonators, tuning the flux bias produces a shift also in the resonator frequencies. From these plots, we obtain the sweet spot of the flux bias as the value corresponding to the maximum qubit frequency, which also coincides with the resonator frequency maxima. Here, the resonance frequencies are the least sensitive for fluctuations in the magnetic flux. Furthermore, we extract the resonance frequencies corresponding to the sweet spot $f_{\mathrm{RO}} = 7.437$ GHz, $f_{\mathrm{Q}} = 3.953$ GHz, and $f_{\mathrm{R}} = 4.671$ GHz for the readout resonator, qubit, and the reset resonator, respectively.

In Fig. 8(a), we can observe a second spectral line below the actual qubit frequency, which suggests that the reset resonator is already weakly excited by thermal photons without any external drive, and induces a dispersive shift to the qubit frequency. The dispersive shift obtained here is $\chi_{\mathrm{R}}/(2\pi) = -2.5$ MHz. We can also observe a parasitic mode in the reset resonator sweep in Fig. 8(b), which is weakly dependent on the flux bias. However, here we are only interested in extracting the main resonance

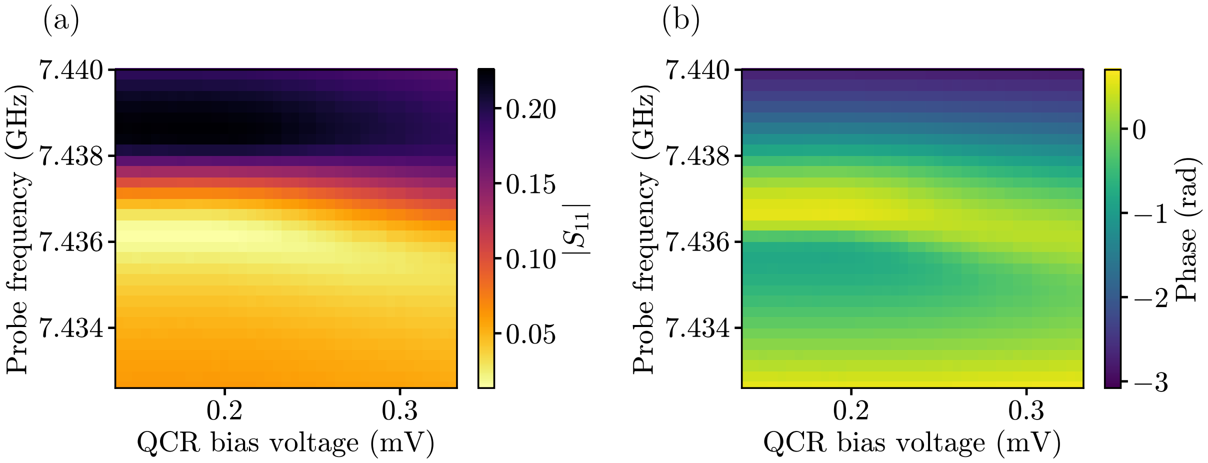

Figure 9: (a) Reflection amplitude and (b) phase response of the readout resonance frequency to the onset of the QCR. When the QCR is dc biased well above the gap voltage $\Delta/e = 203\ \mu$V, the readout resonance frequency shifts slightly towards a lower frequency.

frequency to enable coherent and thermal driving of the resonator.

In the reflection amplitude response of Fig. 8(c), the readout resonance frequency corresponds to the maximum dip at 0 V flux bias, visible as the bright feature, i.e., the minimum reflection amplitude. Above the resonance frequency, the amplitude shoots up, indicating a Fano-type resonance arising from the coupling between the readout resonator and its environment [52]. Comparing with the phase response of Fig. 8(d), we note that the resonance peak in phase is more symmetric and slightly higher in frequency compared to the amplitude response. Thus, the optimal sensing points are determined separately for phase and amplitude to roughly correspond to the respective maximum gradients above the resonance frequencies.

Figure 9 presents the amplitude and phase response of the readout resonator to the onset of the QCR. Above the gap voltage $\Delta/e = 203\ \mu$V, obtained from the IV measurement in Fig. 7, the QCR induces an approximately 1-MHz shift to the resonance frequency of the readout resonator. This effect is possibly a consequence of QCR-induced Lamb shifts on the various resonance frequencies of the coupled system or excitations due to photon-emission-assisted tunneling [24]. Thus, the state of the system slides out from the optimal sensing point, which inflicts the disappearance of the Fock spectral lines into the background, when the QCR is biased above the gap voltage in the two-tone spectroscopy measurements. In order to retain a clear readout signal throughout this bias regime, the induced frequency shift should be compensated during the measurement. However, regarding the aim of these experiments, the relevant phenomena occur slightly below the gap voltage, thus the current measurement protocol suffices for the purposes of this thesis.

As discussed in Sec. 2.5, the quantum state of the reset resonator can be observed by utilizing the two-way dispersive coupling present in this experimental setup, i.e., using the qubit as a probe of the resonator Fock states. The appearance of the Fock spectral lines is demonstrated in Fig. 10(a). Here, the reset resonator is driven with a coherent tone at a drive power of 5 dBm, while sweeping the qubit

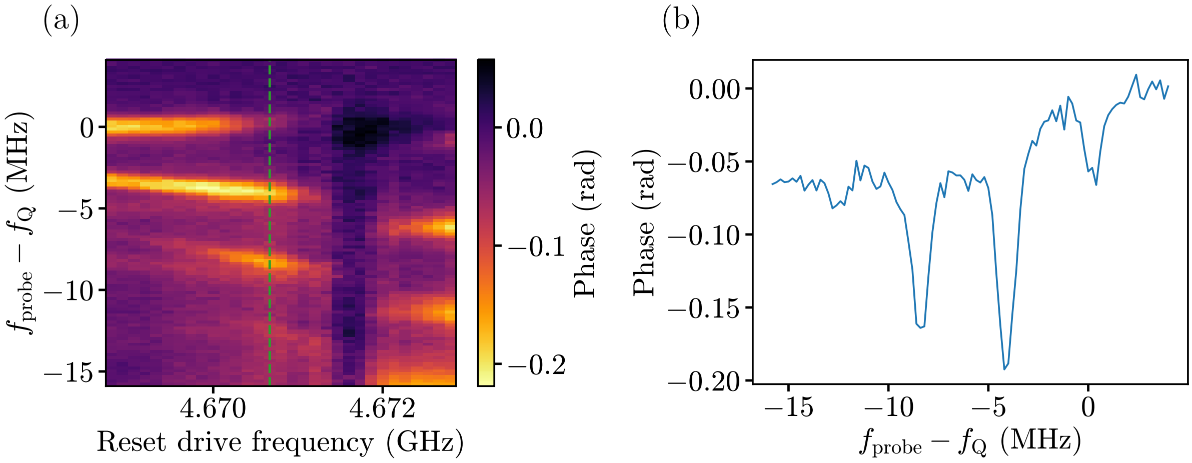

Figure 10: (a) Readout phase response as a function of the qubit probe frequency and the frequency of the coherent drive applied to the reset resonator, at a drive power of 5 dBm. The green dashed line indicates the resonance frequency of the resonator f_{R}. Three dispersively shifted Fock spectral lines, with a spacing slightly changing with the drive frequency, can be distinguished below the base frequency of the qubit f_{Q} corresponding to an empty resonator. (b) Qubit probe frequency spectrum taken at the resonance frequency f_{R}. The dips coincide with the Fock states $|0\rangle$, $|1\rangle$, $|2\rangle$, and $|3\rangle$ of the resonator, from right to left respectively. The amplitude distribution of the dips is consistent with a Poissonian distribution of photons occupying the resonator. The dispersive shift is extracted from the dip splitting as $\chi_{\mathrm{R}}/(2\pi) = -2.2$ MHz.

probe frequency and the resonator drive frequency near the resonance frequencies f_{Q} and f_{R}, respectively. Below the spectral line at the qubit frequency f_{Q} that corresponds to empty occupation on the resonator, three equally spaced spectral lines can be observed, corresponding to photon occupation numbers from 1 to 3. The spacing of the spectral lines varies slightly as a function of drive frequency. Taking into account the second excited state of the transmon qubit, the dispersive shift is given by $2\chi_{\mathrm{R}}/(2\pi) = -\frac{2g^2}{2\pi\Delta_\omega}\frac{\alpha}{\alpha+\Delta_\omega}$, where $\alpha = \omega_{12} - \omega_{01} < 0$ is the transmon anharmonicity [9]. From this expression, we observe that the dispersive shift is inversely proportional to the detuning between the electromagnetic field and the qubit frequency, so the splitting would be expected to decrease towards larger drive frequencies for negative detuning $f_{\mathrm{Q}} < f_{\mathrm{R}}$. The opposite behavior suggests that tuning of the reset resonator drive frequency may induce nontrivial Lamb shifts or ac Stark shifts to the qubit–resonator system, leading to an effective decrease in detuning or increase in anharmonicity. Furthermore, the background phase involves a sudden shift above the resonance frequency, the origin of which remains unidentified.

The subsequent two-tone spectroscopy measurements are carried out with the reset resonator drive frequency tuned at the resonance f_{R}. Figure 10(b) presents the qubit probe frequency spectrum for the coherently driven reset resonator. The Poisson-distributed shape of the dips is readily observed for the Fock states $|0\rangle$, $|1\rangle$, $|2\rangle$, and $|3\rangle$. The mean occupation of photons on the resonator can be visually estimated from the relative depths of the dips to be larger than one.

The mean occupation of the coherently driven resonator can be tuned by adjusting

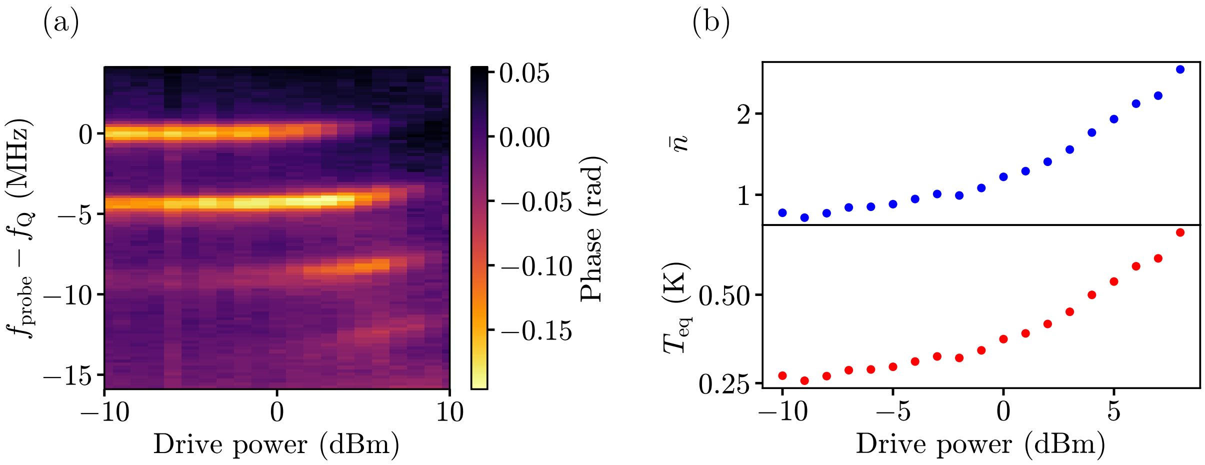

Figure 11: (a) Readout phase response as a function of qubit probe frequency and the drive power of the coherently driven reset resonator. Here, the drive power is varied by tuning the attenuation of the room temperature digital attenuator, see Sec. 4.1. The relative amplitude of the spectral lines corresponding to higher photon occupation increases with the drive power. (b) Mean photon number $\bar{n}$ and equivalent temperature T_{eq} of the reset resonator as a function of the drive power, obtained by fitting a Poissonian distribution to the amplitude distribution of the dips in (a). A distinct increase is visible in both quantities when the drive power is increased.

the drive power, as demonstrated in Fig. 11. For a weak drive, only the first two spectral lines are well visible, the distribution of which would ultimately reduce to a thermal state at a vanishing drive power. When the drive power is increased, the third and the fourth spectral line also appear with increasing amplitude, while the amplitude of the $|0\rangle$ line decreases. Increasing the drive power further initiates a shift in the readout phase, detuning the readout resonator out from the optimal sensing point, and thus, the spectral lines disappear into the background at the largest drive powers in Fig. 11(a).

The increase in the photon number on the reset resonator due to the increased drive strength is further highlighted in Fig. 11(b), which shows the mean photon occupation and equivalent temperature of the reset resonator as a function of the drive power. Here, the data is obtained by fitting the Poisson distribution of Eq. (74) to the minima of the spectral dips in Fig. 11(a), and applying the Bose-Einstein distribution of Eq. (70) to calculate the temperature corresponding to the mean photon number. For a coherent state, this equivalent temperature does not necessarily match with the actual temperature of the system. Within the attainable range of the drive power, the mean occupation of the resonator can be varied by more than one photon, and the equivalent temperature by more than 300 mK.

The effect of a dc-biased QCR on a coherent resonator state is demonstrated in Fig. 12. In the two-tone spectrum of Fig. 12(a), we observe four spectral lines with a Poissonian distribution. The performance of the flux bias source is slightly unstable during the lengthy measurements needed to obtain high-resolution spectra, which inflicts the small fluctuations in the qubit frequency visible here.

When increasing the QCR bias voltage towards the gap voltage $\Delta/e = 203\ \mu\mathrm{V}$,

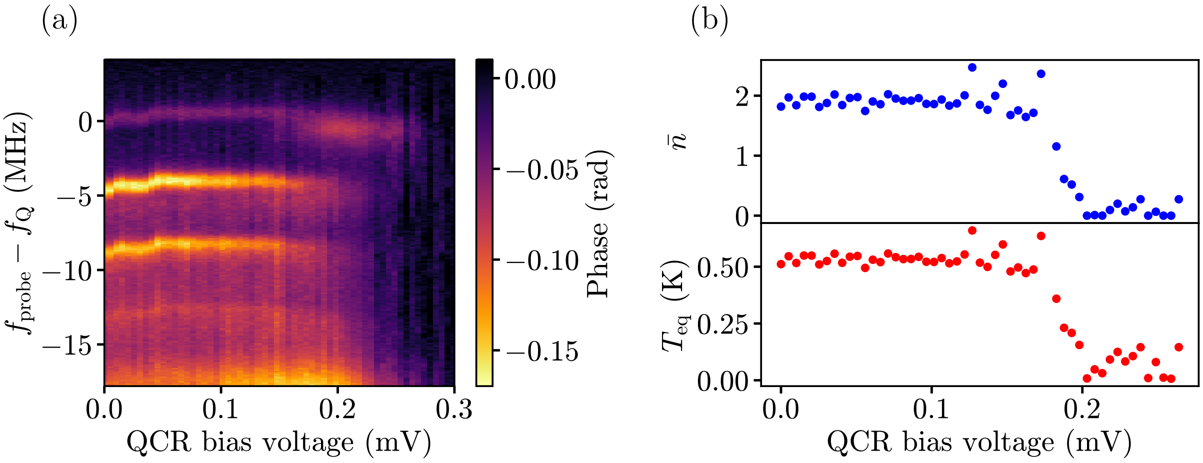

Figure 12: (a) Readout phase response as a function of qubit probe frequency and QCR bias voltage, for the coherently driven reset resonator. At 5-dBm drive power, four spectral lines corresponding to the resonator Fock states can be distinguished, with mean spacing $2\chi_{\mathrm{R}}/(2\pi) = -4.39$ MHz. The dip at the base frequency corresponding to the state $|0\rangle$ of the resonator is weaker than the dips of the states $|1\rangle$ and $|2\rangle$, which distinctly indicates a coherent state rather than a thermal distribution. (b) Mean photon number $\bar{n}$ and equivalent temperature T_{eq} of the reset resonator as a function of QCR bias voltage obtained by fitting a Poisson distribution to the amplitude distribution of the dips in (a). Photon-assisted tunneling through the QCR is activated near the gap voltage $\Delta/e = 203$ μV, which leads to a drop in both the photon number and temperature of the reset resonator.

we observe that the relative magnitude of the three dips corresponding to states $|1\rangle$, $|2\rangle$, and $|3\rangle$ decreases, while the magnitude of the $|0\rangle$ dip increases. Above the gap voltage, the QCR also initiates a shift to the readout frequency, as shown in Fig. 9, and consequently also the $|0\rangle$-state dip disappears to the background. However, the occupation of the higher-photon-number states starts to suppress already below the gap voltage, which is a clear signature of damping of the resonator state by the absorption of photons in a PAT process through the QCR.

The damping effect of the dc-QCR is further elucidated by examining the mean photon number and equivalent temperature in Fig. 12(b). Evidently, the mean photon number and the temperature of the reset resonator remain essentially constant, when the QCR is in the off state, well below the gap voltage. With the bias voltage approaching the gap voltage, the mean photon number decreases quickly to well below the single-photon occupation. Similarly, the equivalent temperature of the resonator drops significantly and remains at a low level for the bias slightly above the gap voltage.

It has been shown in Ref. [25] that the QCR can act as a microwave-photon source that heats the resonator when biased above the gap, due to the onset and domination of the photon-emission-assisted tunneling process, see Fig. 1. In our experiments, up to the bias voltages used here that exceed the gap only slightly, this kind of heating of the resonator state is not visible. Since at higher voltages the spectral lines disappear to the background, observing the heating effect would at

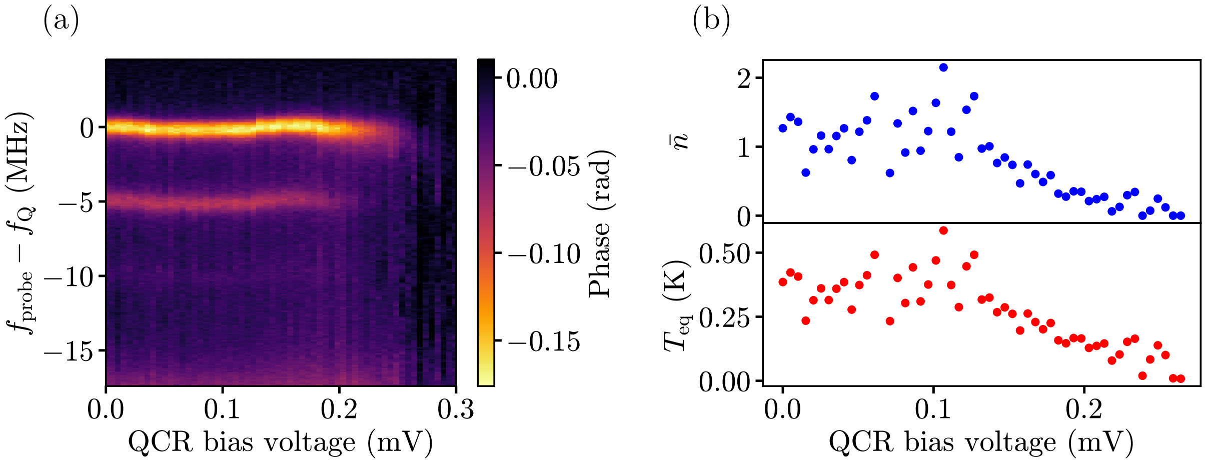

Figure 13: (a) Readout phase response as a function of qubit probe frequency and QCR bias voltage, for a non-driven thermal state of the reset resonator. Three spectral lines can be distinguished with a mean spacing $2\chi_{\text{R}}/(2\pi) = -4.65$ MHz. The state $|0\rangle$ of the resonator corresponds to the base qubit frequency with the most pronounced dip, consistent with the thermal distribution of the Fock states. (b) Mean photon number $\bar{n}$ and equivalent temperature T_{eq} of the reset resonator as a function of QCR bias voltage obtained by fitting a thermal distribution to the amplitude distribution of the dips in (a). Photon-assisted tunneling through the QCR is activated near the gap voltage $\Delta/e = 203$ μV, which leads to a drop in both the photon number and temperature of the reset resonator.

least require a compensation to the shift in the readout frequency to preserve the signal-to-noise ratio (SNR).

Figure 13 shows the effect of the dc-biased QCR on a thermal state of the reset resonator. Here, we can distinguish three spectral lines, corresponding to states $|0\rangle$, $|1\rangle$, and $|2\rangle$. The dip corresponding to state $|0\rangle$ distinctly has the largest depth, which is consistent with the thermal probability distribution given by Eq. (72). Again, we can observe that the two other dispersive lines disappear near the gap voltage, indicating a decrease in the mean photon number and temperature of the resonator.

Similarly as for the coherent state, by fitting the thermal probability distribution to the minima of the dips extracted from Fig. 13(a), we obtain the mean photon number and equivalent temperature of the resonator as a function of QCR bias voltage, presented in Fig. 13(b). Well below the gap voltage, the mean photon number of the thermal state fluctuates more strongly than in the coherent state in Fig. 12(b). Since the data is measured over the course of multiple hours, it is possible that the temperature background of the setup changes slightly between different bias voltage steps, leading to spurious fluctuations that survive the averaging of the frequency sweep traces. On the other hand, the thermal probability distribution is also rather sensitive to small inaccuracies in the extracted dip minima, which may arise during the fitting process or from the random noise remaining in the averaged readout response.

Regardless, for the QCR bias increased towards the gap voltage, we can observe a distinct decrease below the minimum level of the off state for the mean photon number and the equivalent temperature. Thus, Figs. 12 and 13 clearly demonstrate that both a coherent and a thermal state of the reset resonator can be suppressed by a QCR biased with dc voltage.

5.2 Analog frequency-modulated drive of the resonator

In order to investigate the properties of the noise signal generated by the SG396 source, we first analyze its effect on the resonator state. Figure 14 shows the power spectra of the signal generator configured for analog frequency-modulated (AFM) output. That is, the frequency of a sinusoidal carrier signal is modulated by applying additive white Gaussian noise (AWGN) with the largest possible deviation, to obtain maximal noise bandwidth. From Figs. 14(a) and 14(b) we observe that this type of modulation leads to a Gaussian-like shape of the spectrum, with the center frequency corresponding to the respective carrier frequencies 4.671 GHz and 3.600 GHz. For ideal white noise, the power spectrum is expected to be flat over the bandwidth of interest. Here, the flat region is rather concise, however, the spectrum still differs drastically from that of a coherent signal, which would essentially span only a single frequency. In the following experiments, the center frequency of the applied noise is different for the resonator drive and the QCR drive, due to the differences in the filter passbands of the drivelines. However, since the shapes of the respective power spectra are very similar, we can assume that the noise characteristics presented in this section generalize for the QCR drive as well.

Figure 15 presents the effect of the AFM noise on the reset resonator state. In Fig. 15(a), we can observe that a third spectral line appears when noise power is increased around −50 dBm, indicating that the occupation of the resonator increases. However, at high values of noise power, also the qubit linewidth and the dispersive

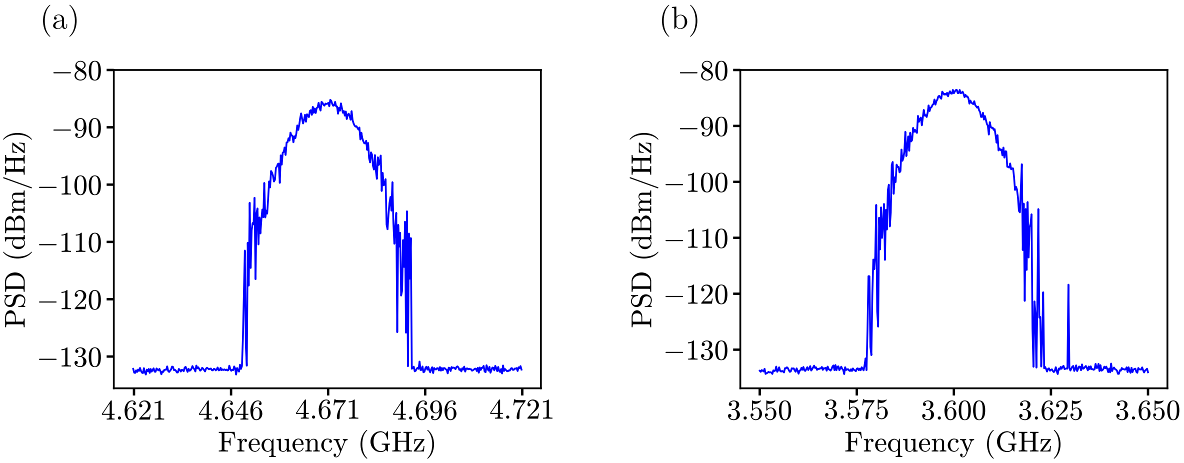

Figure 14: Power spectral density (PSD) of the generated AFM noise, measured by a spectrum analyzer, for carrier frequency (a) 4.671 GHz and (b) 3.600 GHz. The data is averaged over 100 traces, with a resolution bandwidth of 20 kHz. The nominal output power of the signal is −9 dBm. The carrier is frequency-modulated by additive white Gaussian noise with the highest attainable deviation.

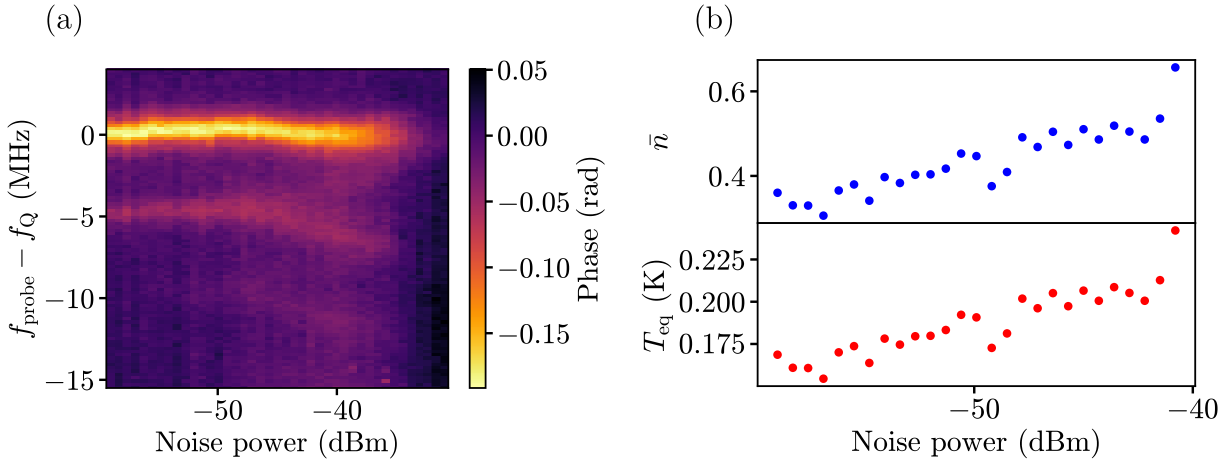

Figure 15: (a) Readout phase response as a function of qubit probe frequency and noise power incident on the reset resonator. The AFM noise has identical configuration parameters to those in Fig. 14(a), but is attenuated and filtered according to the reset driveline parameters, see Table 1. (b) Mean photon number $\bar{n}$ and equivalent temperature T_{eq} of the reset resonator as a function of noise power obtained by fitting a thermal distribution to the amplitude distribution of the dips in (a).

shift increase, which may arise from the strong noise field introducing a secondary ac Stark shift that modifies the observed dispersive shift between the qubit and the reset resonator. The mean photon number and equivalent temperature of the noise-driven resonator, obtained by fitting a thermal distribution to the dips, are shown in Fig. 15(b). Here, we observe a steady increase in both quantities as a function of noise power, suggesting that the AFM noise can be used for heating up the resonator. We also note that the obtained minimum photon number at low noise powers, i.e., a weak noise drive, is smaller than the initial mean occupation of the non-driven thermal state in Fig. 13(b). This might be due to a minor broadening of the Fock spectral lines in the noise-driven case, caused by the readout probe power being slightly increased from the non-driven case. Since the mean photon number given by the thermal distribution is sensitive to small variations in the relative depths of the Fock dips, the small changes in the depth caused by the inhomogeneous broadening of the Fock spectral lines may become significant. Another potential factor for the difference in the initial mean occupation between the two figures is a change in the thermal background during the long time period between the corresponding measurements.

5.3 Analog frequency-modulated drive of the QCR

Following the noise characterization measurements of the previous section, we apply here the noise profile of Fig. 14(b) to the QCR driveline. The center frequency of 3.6 GHz is chosen, since it is the largest applicable frequency that is not significantly attenuated by the cryogenic low-pass filter installed on the driveline.

Figure 16 presents the effect of increased AFM-noise power on the IV curves. Here, we can see a distinct suppression of the gap for drive powers −7 dBm and 0 dBm

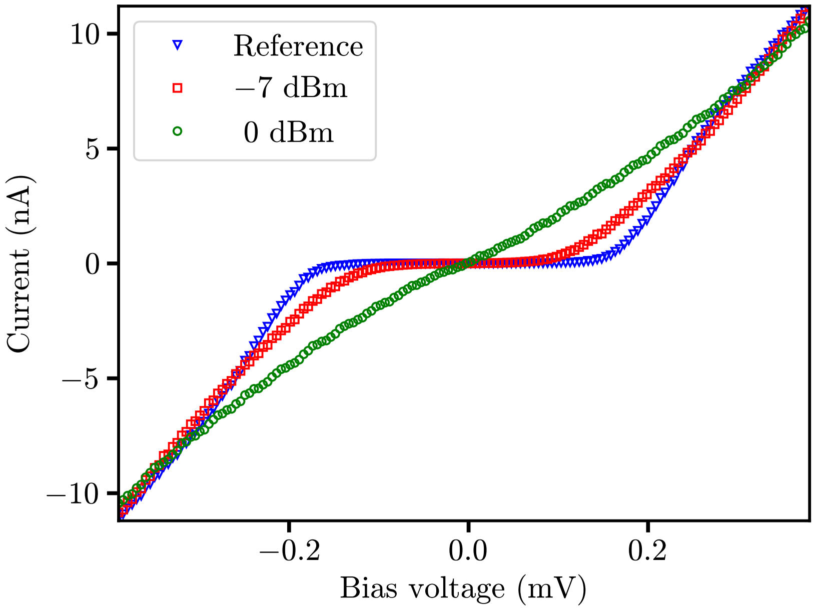

Figure 16: Current through the QCR as a function of its bias voltage for different noise powers of the applied AFM noise. The data are averaged over 10 measurements.

compared to the reference curve. At 0 dBm drive power, the gap has essentially vanished and tunneling is activated without any dc bias.

The effect of AFM-noise-driven QCR on a coherent resonator state is presented in Fig. 17. Besides the offset voltage, no additional dc bias voltage is applied here. In Fig. 17(a), at approximately −1-dBm noise power, an abrupt suppression can be observed for the dips corresponding to finite photon occupation. A similar suppression is visible in Fig. 17(b), in which the mean photon occupation is significanlty reduced, from approximately 1.4 photons to below $\bar{n} = 0.1$. Thus, we conclude that the QCR can be activated purely by noise, with a cooling capability well comparable to the conventional dc-biased QCR. To compare the activation noise power of the QCR with the thermal noise produced by a hot resistor, we insert the full noise bandwidth $B = 47$ MHz and activation power $P_N \approx -1$ dBm extracted from Figs. 14(b) and 17, respectively, and the subsequent nominal attenuation on the QCR line -61.09 dB from Table 1 into Eq. (63), yielding an equivalent noise temperature $T_\mathrm{r} \approx 0.95$ MK. Obviously, this value is infeasible for any practical purposes. In order to realize a Brownian noise drive arising purely from thermal voltage fluctuations, the activation temperature should be minimized by significantly increasing the impedance of the reset resonator and the bandwidth of the noise. For comparison, with a noise bandwidth of $B = 5$ GHz and resistance $R_\mathrm{r} = 5$ kΩ, reaching a root-mean-square voltage equal to the gap voltage $V_\mathrm{r} = 203$ μV would require a more feasible value of $T_\mathrm{r} \approx 30$ K for the temperature of the resistor.

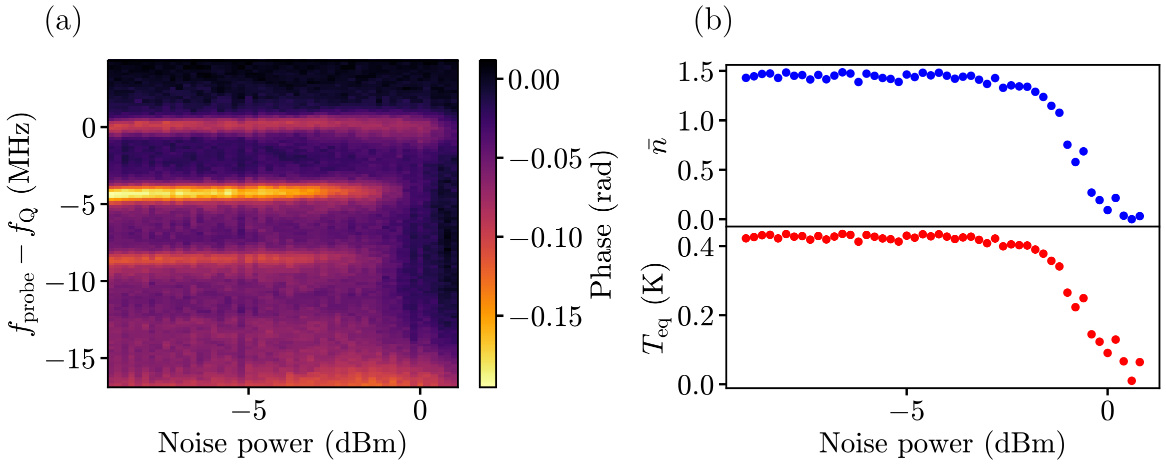

Figure 17: (a) Readout phase response as a function of qubit probe frequency and noise power, for coherently driven reset resonator cooled by AFM-noise-driven QCR. The AFM noise has identical configuration parameters to those in Fig. 14(b), but is attenuated and filtered according to the QCR driveline parameters, see Table 1. No additional dc bias voltage is applied to the QCR. (b) Mean photon number $\bar{n}$ and equivalent temperature T_{eq} of the reset resonator as a function of noise power obtained by fitting a Poisson distribution to the amplitude distribution of the dips in (a).

5.4 Vector frequency-modulated drive

In order to achieve a more thermal-like spectrum for the driving noise, we try another noise configuration given by the SG396 generator, namely vector frequency-modulation (VFM), that modulates the in-phase and quadrature components of the signal, rather than the scalar frequency parameter of the carrier signal as in AFM. Here, the carrier signal is frequency-modulated by a digitally generated pseudo-random binary sequence (PRBS) waveform. The power spectrum of the VFM signal applied in the experiments is shown in Fig. 18. Comparing with the AFM spectra in Fig. 14, the VFM spectrum is flatter around the center frequency, rendering the VFM signal closer to ideal thermal noise. On the other hand, the VFM spectrum has smaller bandwidth compared to AFM and, thus, represents thermal noise in a strongly bandlimited system. The dependence of the shape of the VFM spectrum on the center frequency is negligible, and hence we expect that the essential noise characteristics are retained between the resonator and QCR drive configurations.

Figure 19 presents the effect of the VFM drive on the resonator state for different center frequencies f_{N} of the VFM noise. Due to the limited bandwidth of both the resonator and the noise spectrum, far from the resonance frequency f_{R} the overlap between the two bands is essentially zero, hence the occupation of the resonator is low and the resonator is in a non-driven thermal state. Accordingly, the occupation increases when the resonance frequency enters the noise window and the resonator becomes excited by the additional thermal photons from the drive. This can be observed in Fig. 19(a) as an increase in the amplitude of the second and third

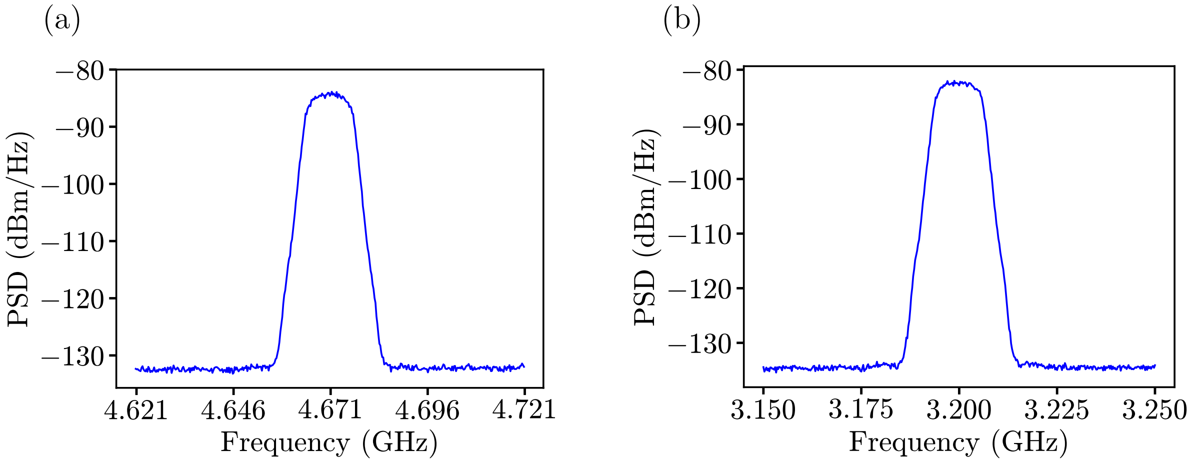

Figure 18: Power spectral density of the generated VFM noise, measured by a spectrum analyzer, for carrier frequency (a) 4.671 GHz and (b) 3.200 GHz. The data is averaged over 100 traces, with a resolution bandwidth of 20 kHz. The nominal output power of the signal is −9 dBm. The carrier is modulated by a PRBS-noise waveform with the highest attainable deviation.

spectral line. The heating effect of the noise is not perfectly symmetric about the resonance frequency f_R, which is possibly related to the asymmetry of the resonance dip of the resonator, see Fig. 8(b). That is, the resonance has a sharp edge on the low-frequency side but a longer tail on the high-frequency side, so thermal excitation is allowed for a larger detuning in the positive direction. The mean photon number

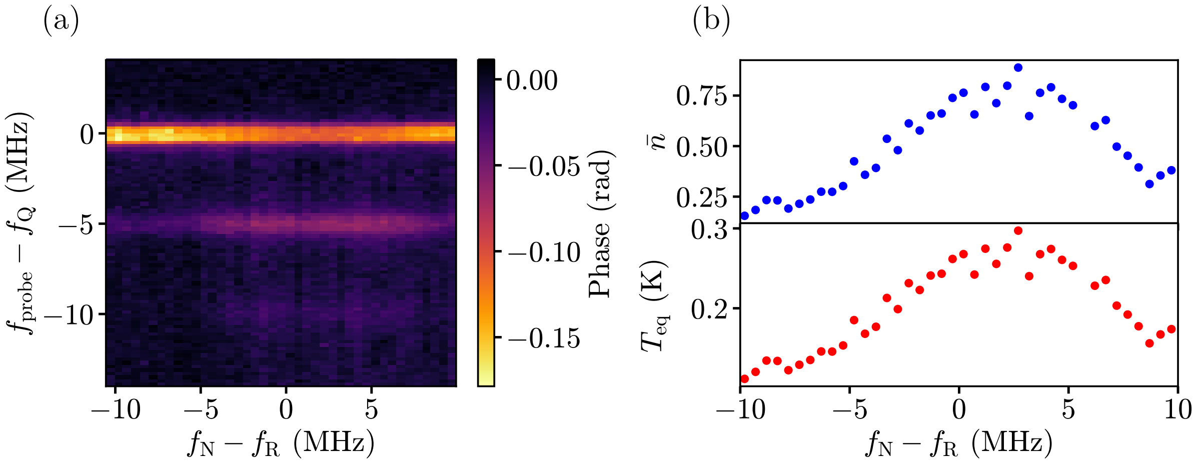

Figure 19: (a) Readout phase response as a function of qubit probe frequency and the normalized center frequency of the noise, for VFM noise incident on the reset resonator at −43-dBm noise power. The noise has identical configuration parameters to those in Fig. 18(a), but is attenuated and filtered according to the reset drive line parameters, see Table 1. (b) Mean photon number $\bar{n}$ and equivalent temperature T_{eq} of the reset resonator as a function of normalized noise frequency obtained by fitting a thermal distribution to the amplitude distribution of the dips in (a).

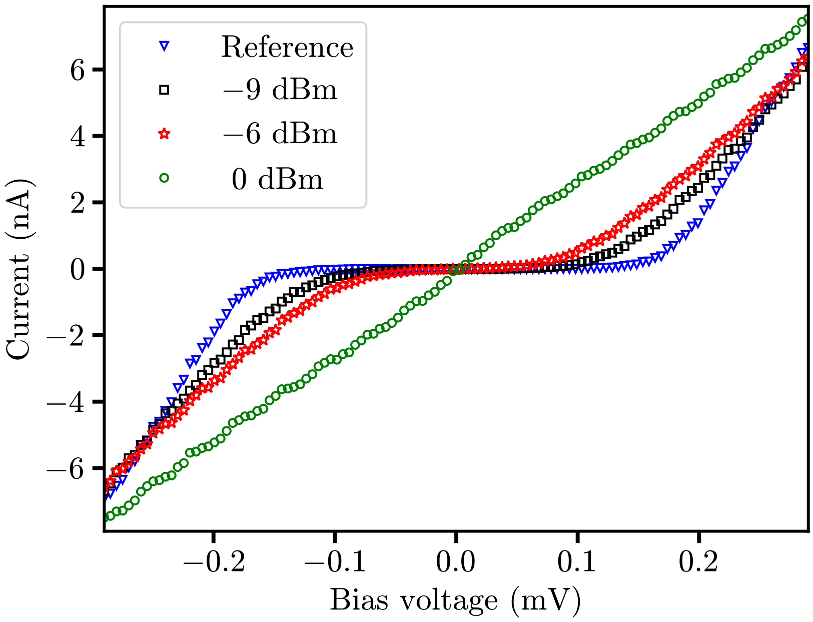

Figure 20: Current through the QCR as a function of its bias voltage for different noise powers of the applied VFM noise. The data are averaged over 10 measurements.

and equivalent temperature in Fig. 19(b), obtained by fitting a thermal distribution to the dips, show a similar increase near the resonance frequency.

The effect of the VFM noise on the current–voltage characteristics of the QCR is shown in Fig. 20. Similarly as for the analog modulation in Fig. 16, we observe a suppression of the superconductor gap with increasing noise power. Thus, we conclude that also VFM noise can activate the photon-assisted tunneling without additional bias voltage. The small jumps in current at $|V| > \Delta/e$ are likely related to grounding instabilities in the system, since they occur across the complete bias voltage range, and can also be observed to some extent in some other QCR samples not presented here.

Figure 21(a) presents the two-tone spectroscopy of a non-driven thermal resonator state cooled by VFM-noise-driven QCR. Here, the digital attenuation of the qubit drive is slightly decreased compared to the configuration in Figs. 15 and 19, resulting in a small increase in the background thermal occupation of the resonator. In contrast to the other two-tone measurements presented in this thesis, here we have measured the amplitude response instead of phase, due to issues with the flux bias voltage source, inducing fluctuations that corrupt the phase signal. The amplitude signal involves a frequency-dependent background, which slightly degrades the third and fourth spectral lines, inducing some error to the fit of the thermal distribution. Since Fig. 21(a) is already obtained without applying any drive on the resonator, measuring only the background separately from the spectral lines sets a challenge that is not explored further in this case.

Despite the effect of the frequency-dependent background, we can observe in Fig. 21(a) the suppression of the second and third spectral line near 0-dBm noise

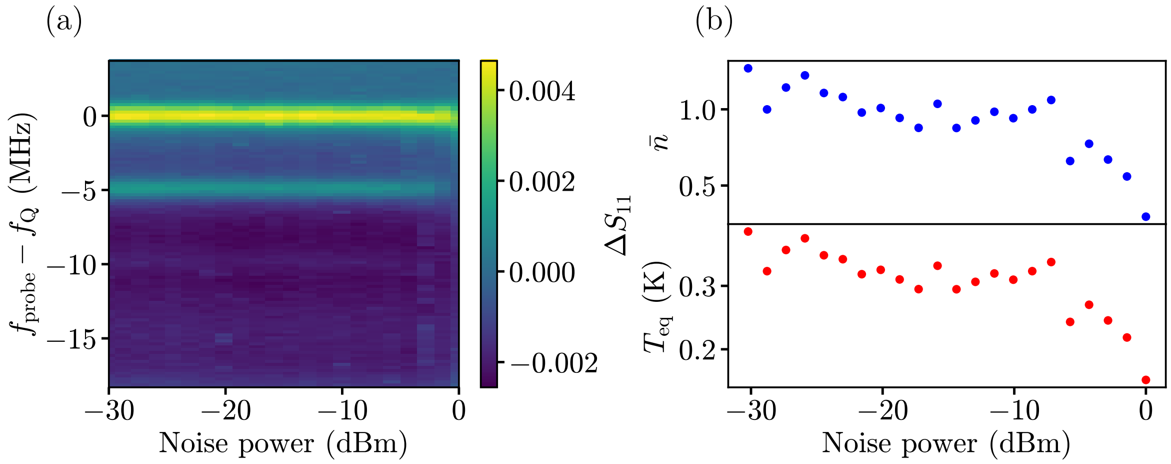

Figure 21: (a) Readout amplitude response as a function of qubit probe frequency and noise power, for non-driven reset resonator cooled by VFM-noise-driven QCR. The VFM noise has identical configuration parameters to those in Fig. 18(b), but is attenuated and filtered according to the QCR line parameters, see Table 1. No additional dc bias voltage is applied to the QCR. (b) Mean photon number $\bar{n}$ and temperature T_{eq} of the reset resonator as a function of noise power obtained by fitting a thermal distribution to the amplitude distribution of the peaks in (a).

power. The suppression of the mean photon number and equivalent temperature is visible in Fig. 21(b), in which $\bar{n} \approx 1$ at low noise powers, but decreases below $\bar{n} = 0.5$ at 0-dBm noise power. Thus, these results suggest that also a thermal non-driven state of the resonator can be cooled by a noise-driven QCR, which is the essence of the QBR concept. Similarly as found for the AFM-noise case, replacing the artificial noise drive with a Brownian source, such as the hot resistor introduced in Sec. 2.4, would require a high-impedance circuit to obtain a sufficient noise power to activate the QCR. Since the artificial noise used here is strongly bandlimited, adjusting the filtering and utilizing wide-band Brownian noise would allow for a lower activation power.

6 Summary and outlook

In conclusion, we have demonstrated the damping and cooling of a coherent and a thermal resonator state by a noise-driven quantum-circuit refrigerator. The composition of the resonator state was conveniently accessed by exploiting a transmon qubit as a dispersive probe. The amplitude distribution of the ac-Stark-shifted spectral lines was utilized for extracting information on the distribution of the Fock states and the mean number of photons in the resonator.

To enhance the accuracy of the fitting of photon distributions in the future, it may be beneficial to consider extracting the area of the spectral dips to compensate for the inhomogeneous broadening and flattening of the dips that depends on the photon number. Furthermore, the setup can be optimized in such way that it allows for the observation of higher-photon-number states, so that more datapoints can be obtained for the fit. To obtain a better visualization of the resonator state well above the gap voltage, the observed shift in the resonance frequency of the readout resonator should be compensated for.

By applying analog and vector frequency-modulated noise signal to the resonator, we showed an increase in the mean photon occupation, equivalent to the heating of the resonator. Identical noise waveforms, apart from the center frequency, were then applied to the QCR, resulting in the activation of photon-assisted tunneling in the absence of any additional dc bias voltage. This activation was observed as the suppression of the zero-current plateau arising from the superconductor gap in the current–voltage characteristics, and as the evident decrease in the mean photon occupation of the resonator to well below a single photon as a function of noise power.

A natural step following the demonstrated cooling by the noise-driven QCR would be to replace the artificial noise generator used here by a passive noise source, such as a hot resistor. In the current setup, the equivalent noise temperature of a resistor required to activate the QCR is well beyond the practical limits of the setup, implying that significant modifications to the impedance and bandwidth parameters of the system are necessary, in order to lower the equivalent noise temperature to reasonable values.

The potential of the QCR–resonator combination in Brownian quantum-circuit refrigeration is not limited to the configuration studied in this thesis. As we demonstrated here, driving the resonator instead of the QCR by noise results in an increase in the thermal population of the driven resonator mode. By utilizing two modes of a resonator, the secondary mode can assist in the cooling of the primary mode by supplying high-energy photons to the QCR that partially replace the dc bias voltage. Combining the Brownian noise from a hot resistor as the drive with a high-impedance resonator that provides high-energy photons to the QCR, this type of system would constitute a promising platform for the realization of a quantum Brownian refrigerator operating purely by thermal power.

References

[1] P. Benioff, Quantum mechanical models of Turing machines, Journal of Statistical Physics **29**, 515 (1982).

[2] R. P. Feynman, Quantum mechanical computers, Optics News **11**, 11 (1985).

[3] A. K. Fedorov, N. Gisin, S. M. Beloussov, and A. I. Lvovsky, Quantum computing at the quantum advantage threshold: a down-to-business review, arXiv:2203.17181 (2022).

[4] F. Arute, K. Arya, R. Babbush, *et al.*, Quantum supremacy using a programmable superconducting processor, Nature **574**, 505 (2019).

[5] S. S. Gill, A. Kumar, H. Singh, M. Singh, K. Kaur, M. Usman, and R. Buyya, Quantum computing: A taxonomy, systematic review and future directions, Software: Practice and Experience **52**, 66 (2022).

[6] A. D. Corcoles, A. Kandala, A. Javadi-Abhari, D. T. McClure, A. W. Cross, K. Temme, P. D. Nation, M. Steffen, and J. M. Gambetta, Challenges and opportunities of near-term quantum computing systems, Proceedings of the IEEE **108**, 1338 (2020).

[7] W. P. Schleich, K. S. Ranade, C. Anton, *et al.*, Quantum technology: from research to application, Applied Physics B **122**, 130 (2016).

[8] H. L. Huang, D. Wu, D. Fan, and X. Zhu, Superconducting quantum computing: a review, Science China Information Sciences **63**, 180501 (2020).

[9] P. Krantz, M. Kjaergaard, F. Yan, T. P. Orlando, S. Gustavsson, and W. D. Oliver, A quantum engineer's guide to superconducting qubits, Applied Physics Reviews **6**, 021318 (2019).

[10] M. D. Reed, B. R. Johnson, A. A. Houck, L. Dicarlo, J. M. Chow, D. I. Schuster, L. Frunzio, and R. J. Schoelkopf, Fast reset and suppressing spontaneous emission of a superconducting qubit, Applied Physics Letters **96**, 203110 (2010).

[11] N. Ofek, A. Petrenko, R. Heeres, *et al.*, Extending the lifetime of a quantum bit with error correction in superconducting circuits, Nature **536**, 441 (2016).

[12] J. Tuorila, M. Partanen, T. Ala-Nissila, and M. Möttönen, Efficient protocol for qubit initialization with a tunable environment, npj Quantum Information **3**, 27 (2017).

[13] M. T. Mitchison, Quantum thermal absorption machines: refrigerators, engines and clocks, Contemporary Physics **60**, 164 (2019).

[14] J. B. Brask, G. Haack, N. Brunner, and M. Huber, Autonomous quantum thermal machine for generating steady-state entanglement, New Journal of Physics **17**, 113029 (2015).

[15] N. Linden, S. Popescu, and P. Skrzypczyk, How small can thermal machines be? The smallest possible refrigerator, Physical Review Letters **105**, 130401 (2010).

[16] H. T. Quan, Y. X. Liu, C. P. Sun, and F. Nori, Quantum thermodynamic cycles and quantum heat engines, Physical Review E **76**, 031105 (2007).

[17] J. P. Pekola and F. W. J. Hekking, Normal-metal-superconductor tunnel junction as a Brownian refrigerator, Physical Review Letters **98**, 210604 (2007).

[18] C. V. D. Broeck and R. Kawai, Brownian refrigerator, Physical Review Letters **96**, 210601 (2006).

[19] K. Y. Tan, M. Partanen, R. E. Lake, J. Govenius, S. Masuda, and M. Möttönen, Quantum-circuit refrigerator, Nature Communications **8**, 15189 (2017).

[20] M. Silveri, H. Grabert, S. Masuda, K. Y. Tan, and M. Möttönen, Theory of quantum-circuit refrigeration by photon-assisted electron tunneling, Physical Review B **96**, 094524 (2017).

[21] M. Silveri, S. Masuda, V. Sevriuk, *et al.*, Broadband Lamb shift in an engineered quantum system, Nature Physics **15**, 533 (2019).

[22] V. A. Sevriuk, K. Y. Tan, E. Hyyppä, *et al.*, Fast control of dissipation in a superconducting resonator, Applied Physics Letters **115**, 082601 (2019).

[23] A. Viitanen, M. Silveri, M. Jenei, *et al.*, Photon-number-dependent effective Lamb shift, Physical Review Research **3**, 033126 (2021).

[24] A. Viitanen, T. Mörstedt, W. S. Teixeira, M. Tiiri, J. Räbinä, M. Silveri, and M. Möttönen, Quantum-circuit refrigeration of a superconducting microwave resonator well below a single quantum, arXiv:2308.00397 (2023).

[25] S. Masuda, K. Y. Tan, M. Partanen, R. E. Lake, J. Govenius, M. Silveri, H. Grabert, and M. Möttönen, Observation of microwave absorption and emission from incoherent electron tunneling through a normal-metal-insulator-superconductor junction, Scientific Reports **8**, 3966 (2018).

[26] V. A. Sevriuk, W. Liu, J. Rönkkö, *et al.*, Initial experimental results on a superconducting-qubit reset based on photon-assisted quasiparticle tunneling, Applied Physics Letters **121**, 234002 (2022).

[27] T. Yoshioka, H. Mukai, A. Tomonaga, S. Takada, Y. Okazaki, N.-H. Kaneko, S. Nakamura, and J.-S. Tsai, Active initialization experiment of superconducting qubit using quantum-circuit refrigerator, arXiv:2306.10212 (2023).

[28] V. Vadimov, A. Viitanen, T. Mörstedt, T. Ala-Nissila, and M. Möttönen, Single-junction quantum-circuit refrigerator, AIP Advances **12**, 075005 (2022).

[29] T. F. Mörstedt, A. Viitanen, V. Vadimov, V. Sevriuk, M. Partanen, E. Hyyppä, G. Catelani, M. Silveri, K. Y. Tan, and M. Möttönen, Recent developments in quantum-circuit refrigeration, Annalen der Physik **534**, 2100543 (2022).

[30] N. Zettili, *Quantum mechanics: Concepts and applications*, 2nd ed. (John Wiley & Sons, Chichester, 2009) pp. 227–231.

[31] K. Gloos, P. J. Koppinen, and J. P. Pekola, Properties of native ultrathin aluminium oxide tunnel barriers, Journal of Physics: Condensed Matter **15**, 1733 (2003).

[32] D. R. Jennison, C. Verdozzi, P. A. Schultz, and M. P. Sears, Ab initio structural predictions for ultrathin aluminum oxide films on metallic substrates, Physical Review B **59**, R15605 (1999).

[33] J. Bardeen, L. N. Cooper, and J. R. Schrieffer, Microscopic theory of superconductivity, Physical Review **106**, 162 (1957).

[34] G.-L. Ingold and Y. V. Nazarov, Charge tunneling rates in ultrasmall junctions, in *Single Charge Tunneling, NATO ASI Series B*, Vol. 294, edited by H. Grabert and M. H. Devoret (1992) pp. 21–107.

[35] J. P. Pekola, V. F. Maisi, S. Kafanov, N. Chekurov, A. Kemppinen, Y. A. Pashkin, O.-P. Saira, M. Möttönen, and J. S. Tsai, Environment-assisted tunneling as an origin of the Dynes density of states, Physical Review Letters **105**, 026803 (2010).

[36] F. Herman and R. Hlubina, Microscopic interpretation of the Dynes formula for the tunneling density of states, Physical Review B **94**, 144508 (2016).

[37] R. C. Dynes, J. P. Garno, G. B. Hertel, and T. P. Orlando, Tunneling study of superconductivity near the metal-insulator transition, Physical Review Letters **53**, 2437 (1984).

[38] H. Hsu, M. Silveri, V. Sevriuk, M. Möttönen, and G. Catelani, Charge dynamics in quantum-circuit refrigeration: Thermalization and microwave gain, AVS Quantum Science **3**, 042001 (2021).

[39] A. Blais, A. L. Grimsmo, S. M. Girvin, and A. Wallraff, Circuit quantum electrodynamics, Reviews of Modern Physics **93**, 025005 (2021).

[40] M. H. Devoret, Quantum fluctuations in electrical circuits, in *Les Houches, Session LXIII 7.8* (1995) pp. 353–386.

[41] K. E. Cahill and R. J. Glauber, Ordered expansions in boson amplitude operators, Physical Review **177**, 1857 (1969).

[42] M. Abramowitz and I. A. Stegun, *Handbook of mathematical functions with formulas, graphs and mathematical tables*, 10th ed. (US Government Printing Office, Washington, 1972) pp. 773–800.

[43] G. Schön, Single-electron tunneling, in *Quantum Transport and Dissipation* (Wiley-VCH, Weinheim, 1997) pp. 149–212.

[44] H. Hsu, Quantum circuit refrigerator for superconducting circuits : qubit reset and microwave gain, Ph.D thesis, RWTH Aachen University 10.18154/RWTH-2021-11569 (2021).

[45] D. M. Pozar, *Microwave engineering*, 4th ed. (John Wiley & Sons, Hoboken, 2012) pp. 498–501.

[46] B. W. Shore and P. L. Knight, The Jaynes–Cummings model, Journal of Modern Optics **40**, 1195 (1993).

[47] D. Zueco, G. M. Reuther, S. Kohler, and P. Hänggi, Qubit-oscillator dynamics in the dispersive regime: Analytical theory beyond the rotating-wave approximation, Physical Review A **80**, 033846 (2009).

[48] M. O. Scully and A. A. Svidzinsky, The Lamb shift – Yesterday, today, and tomorrow, Science **328**, 1239 (2010).

[49] A. Fragner, M. Göppl, J. M. Fink, M. Baur, R. Bianchetti, P. J. Leek, A. Blais, and A. Wallraff, Resolving vacuum fluctuations in an electrical circuit by measuring the Lamb shift, Science **322**, 1357 (2008).

[50] D. I. Schuster, A. A. Houck, J. A. Schreier, *et al.*, Resolving photon number states in a superconducting circuit, Nature **445**, 515 (2007).

[51] A. D. Marco, V. F. Maisi, J. P. Pekola, and F. W. J. Hekking, Leakage current of a superconductor-normal metal tunnel junction connected to a high-temperature environment, Physical Review B **88**, 174507 (2013).

[52] J. Leppäkangas, J. D. Brehm, P. Yang, L. Guo, M. Marthaler, A. V. Ustinov, and M. Weides, Resonance inversion in a superconducting cavity coupled to artificial atoms and a microwave background, Physical Review A **99**, 063804 (2019).